scientific reports

OPEN

Integrative in silico and in vivo Drosophila model studies reveal the anti-inflammatory, antioxidant, and anticancer properties of red radish microgreen extract

Trina Ekawati Tallei[1,2✉], Nova Hellen Kapantow[3], Nurdjannah Jane Niode[4], Sofia Safitri Hessel[5], Maghfirah Savitri[6], Fatimawali Fatimawali[7], Sojin Kang[8,9], Moon Nyeo Park[8,9], Muhammad Raihan[10], Widya Hardiyanti[11], Firzan Nainu[11,12] & Bonglee Kim[8,9✉]

Red radish microgreens (RRM) have gained considerable attention for their promising therapeutic potential. However, the molecular mechanisms underlying their bioactivity remain inadequately characterized. This study explores the anti-inflammatory, antioxidant, and anticancer properties of RRM extract using in silico and in vivo Drosophila model analyses. The metabolite profile of the RRM extract was characterized using comprehensive metabolomics techniques, including Gas Chromatography-Mass Spectrometry (GC-MS) and Liquid Chromatography High-Resolution Mass Spectrometry (LC-HRMS). Furthermore, in silico analysis utilizing network pharmacology identified target proteins of RRM compounds associated with cancer, inflammation, and oxidative stress. Concurrently, in vivo experiments with *Drosophila melanogaster PGRP-LB*$^\Delta$ (Dm *PGRP-LB*$^\Delta$) larvae was conducted to assess the extract's impact on immune and oxidative stress pathways. In silico analysis revealed that RRM compounds interacted with key proteins (AKT1, ESR1, MAPK1, SRC, TP53), modulating pathways related to cancer, inflammation, and oxidative stress. Molecular dynamics simulations reinforced the docking results by confirming robust binding of kaempferitrin to AKT1. In vivo studies showed that RRM extract suppressed immune-related genes (*dptA*, *totA*) through the NFκB and JAK-STAT pathways, reduced ROS levels, and selectively regulated antioxidant gene expression by enhancing *sod1* while decreasing *sod2 and cat*. These results suggest RRM extract as a functional food for managing oxidative stress, inflammation, and cancer. Further research in higher organisms and clinical settings is needed.

Keywords Red radish microgreens, Functional food, *Drosophila*, Network Pharmacology, Molecular mechanisms

[1]Department of Biology, Faculty of Mathematics and Natural Sciences, Sam Ratulangi University, Manado 95115, North Sulawesi, Indonesia. [2]Department of Biology, Faculty of Medicine, Sam Ratulangi University, Manado 95115, North Sulawesi, Indonesia. [3]Department of Nutrition, Faculty of Medicine, Sam Ratulangi University, Manado 95115, North Sulawesi, Indonesia. [4]Department of Dermatology and Venereology, Faculty of Medicine, Sam Ratulangi University, Prof. Dr. R.D. Kandou Hospital Manado, Manado 95115, North Sulawesi, Indonesia. [5]Department of Biotechnology, Indonesia Biodiversity and Biogeography Research Institute (INABIG), Bandung 40132, West Java, Indonesia. [6]Faculty of Medicine, Sam Ratulangi University, Manado 95115, North Sulawesi, Indonesia. [7]Pharmacy Study Program, Faculty of Mathematics and Natural Sciences, Sam Ratulangi University, Manado 95115, North Sulawesi, Indonesia. [8]Department of Pathology, College of Korean Medicine, Kyung Hee University, Hoegidong Dongdaemun-gu, Seoul 02447, South Korea. [9]Korean Medicine-Based Drug Repositioning Cancer Research Center, College of Korean Medicine, Kyung Hee University, Seoul 02447, South Korea. [10]Department of Pharmaceutical Science and Technology, Faculty of Pharmacy, Universitas Hasanuddin, Tamalanrea 90245, Makassar, Indonesia.

[11]Faculty of Pharmacy, UNHAS Fly Research Group, Hasanuddin University, Tamalanrea 90245, Makassar, Indonesia. [12]Department of Pharmacy, Faculty of Pharmacy, Universitas Hasanuddin, Tamalanrea 90245, Makassar, Indonesia. ✉email: trina_tallei@unsrat.ac.id; bongleekim@khu.ac.kr

Microgreens, the young shoots of vegetables and herbs, are recognized for their rich concentration of bioactive compounds with notable health benefits. Among these, red radish (*Raphanus sativus* var. sativus) microgreens have gained attention due to their high levels of bioactive compounds with numerous health benefits. Research has demonstrated that these compounds modulate key biological pathways related to oxidative stress, inflammation, and carcinogenesis, highlighting the potential of red radish microgreens (RRM) in functional food development[1].

Red radish has long been valued for its health benefits, particularly due to bioactive compounds like glucosinolates, isothiocyanates, and sulforaphane[2]. These compounds play crucial roles in detoxifying carcinogens, inhibiting tumor growth, and contributing to antioxidant activity by scavenging free radicals and reducing oxidative damage, a key factor in chronic inflammation and cancer progression. Red radish microgreens retain these properties, further establishing their potential as a functional food with anti-inflammatory[3] and anticancer[4] activities.

Despite existing findings, significant gaps remain in understanding the molecular mechanisms driving the anti-inflammatory and anticancer effects of red radish microgreens. Most studies have relied on in vitro assays[5–7], with limited use of omics approaches or advanced computational methods to predict molecular interactions. This study aims to address these gaps by employing a multidisciplinary approach that integrates metabolomics, in silico analyses, and preclinical validation. Metabolomics will provide a comprehensive profile of bioactive compounds in RRM and their roles in metabolic pathways, overcoming the limitations of analyzing individual compounds. In silico analyses will predict how these compounds interact with antioxidant-, inflammation- and cancer-related targets, offering mechanistic insights. Finally, preclinical validation using *Drosophila* models will assess the biological relevance of these findings, ensuring their practical application in health contexts.

Computer methods have emerged as an important tool in new drug discovery, enabling scientists to screen large compound libraries efficiently and predict how they will interact with target proteins. Techniques such as molecular docking, virtual screening, and network pharmacology simulate drug-target interactions at the molecular level, thereby accelerating the discovery and optimization of promising lead compounds[8–12]. Furthermore, the application of machine learning techniques has been employed to enhance these predictions, supporting the development of therapies with multiple targets and speeding the drug development process[13,14].

Preclinical drug testing necessitates appropriate model organisms, but ethical concerns regarding traditional animals like mice and rats are increasing. *Drosophila melanogaster*, the fruit fly, presents a promising alternative with a long history in research, including studies on neurodegenerative diseases and metabolic syndromes[15,16]. Sharing approximately 60% genetic similarity with humans, *D. melanogaster* serves as a valuable model for studying human diseases. Up to 75% of human disease-related genes have an ortholog in *Drosophila*[17], enabling researchers to develop disease models through genetic manipulation or chemical induction. Specialized tools can further predict orthologous genes based on sequence, expression patterns, and function, reinforcing Drosophila's role in biomedical research[18]. Moreover, Drosophila has been widely used to study inflammatory pathways, oxidative stress responses, and cancer-related mechanisms due to its conserved immune signaling pathways, including Toll, immune deficiency and JAK/STAT, which closely resemble those in humans[19,20]. It has also served as an alternative model organism in nutrigenomics research[21]. Studies have shown that *Drosophila* can effectively model chronic inflammation, tumor progression, and oxidative stress-related diseases, making it a valuable system for evaluating the therapeutic potential of bioactive compounds[22].

In this study, the anti-inflammatory potential of RRM extract was tested in vivo using the PGRP-LB$^\Delta$ mutant of *D. melanogaster*. The aim is to evaluate the anti-inflammatory, antioxidant, and anticancer properties of RRM by identifying bioactive compounds, elucidating their mechanisms of action, and validating their therapeutic potential for disease prevention and therapy.

Results

Chemical composition and multi-target gene network analysis of RRM bioactive compounds

LC-HRMS and GC-MS analyses reveal a diverse chemical profile of RRM compounds. Specifically, 40 compounds were detected via GC-MS and 191 via LC-MS, yielding a total of 231 compounds. After applying filtering criteria, 141 compounds remained. These were then categorized into various chemical groups (Fig. 1): lipids represented the largest group (24.7%), followed by phenolic compounds (16.0%) and amino acids with their derivatives (12.3%). Additionally, heterocyclic compounds (11.1%), fatty acyls (6.2%), and smaller fractions of vitamins, terpenes, alkaloids, and other classes (ranging from 2.5 to 4.9%) further underscore the chemical diversity.

A total of 141 filtered compounds were subsequently utilized to target genes associated with cancer, inflammation, and oxidative stress. The analysis identified 7,645 target genes corresponding to the bioactive compounds in RRM, which were then refined to 1,173 unique genes after removing duplicates. From the GeneCards database, 30,554 cancer-related genes, 16,357 inflammation-associated genes, and 14,285 oxidative stress-related genes were retrieved. After merging these datasets and eliminating redundancies, a total of 35,910 unique genes implicated in these biological processes were obtained. A Venn diagram analysis identified 1,154 overlapping genes that serve as common targets of RRM compounds and are associated with cancer, inflammation, and oxidative stress. This significant overlap underscores the multitargeting potential of RRM bioactive compounds, highlighting their ability to modulate interconnected pathways involved in these conditions. These overlapping genes were prioritized for further investigation, as illustrated in Fig. 2.

Protein-protein interaction (PPI) analysis was conducted for the 1,154 target proteins using a stringent interaction score threshold of 0.900 to ensure high-confidence results. The resulting network, visualized in
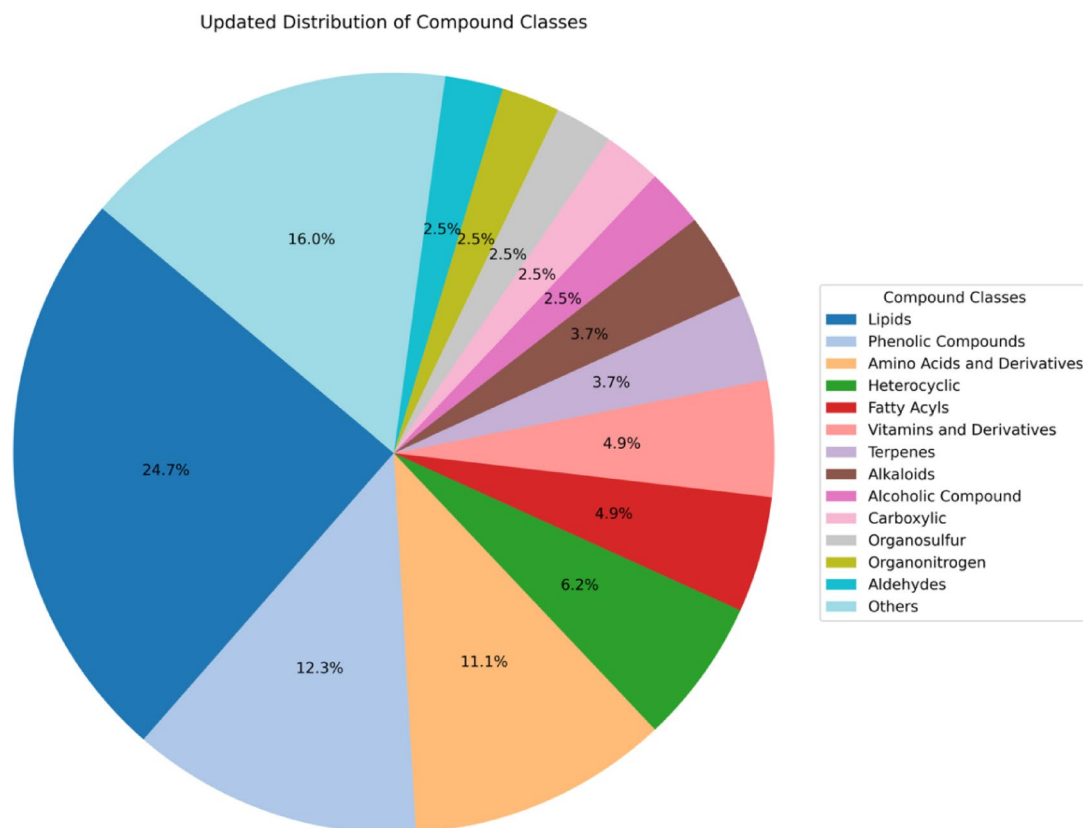
Fig. 1. Classification of RRM compounds identified via LC-HRMS and GC-MS analyses, categorized based on their chemical classes.
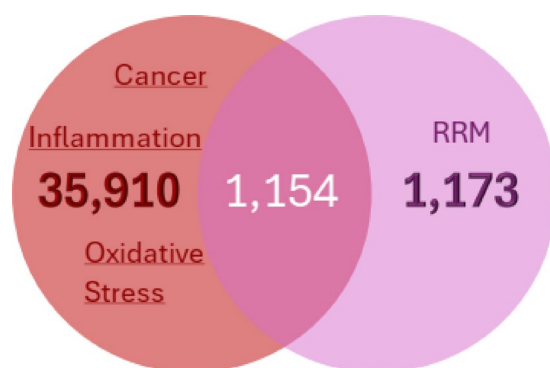

Fig. 2. Venn diagram illustrating the overlapping target genes between RRM compounds and genes associated with cancer, inflammation, and oxidative stress.

Supplementary File 1, comprises 869 targets interconnected by 3,760 interactions. Further network evaluation included centrality analyses, calculating degree, betweenness, closeness, and stress centralities to determine key regulatory nodes. The CytoHubba plugin, utilizing maximum neighborhood component (MNC) and maximal clique centrality (MCC) algorithms, identified 32 key RRM-targeted genes implicated in cancer, inflammation, and oxidative stress. The integrated network (Fig. 3) and centrality rankings (Table 1) highlight significant targets based on multiple topological metrics. Among these, TP53 emerged as the most central node, exhibiting the highest stress centrality (1,575,862), degree (97), and betweenness (0.16580), reinforcing its crucial role in cancer and oxidative stress pathways.

The skyline analysis (Fig. 4) identified TP53, SRC, AKT1, MAPK1, and ESR1 as the top five key proteins, consistent with rankings obtained from MNC and MCC scores. Among them, TP53 exhibited the highest centrality metrics, including a betweenness centrality of 0.16580, closeness centrality of 0.36032, degree of 97, and stress centrality of 1,575,862, underscoring its pivotal role in network organization. Furthermore, 49 compounds were predicted to interact with these key proteins. Among them, five—kaempferitrin, alpha-
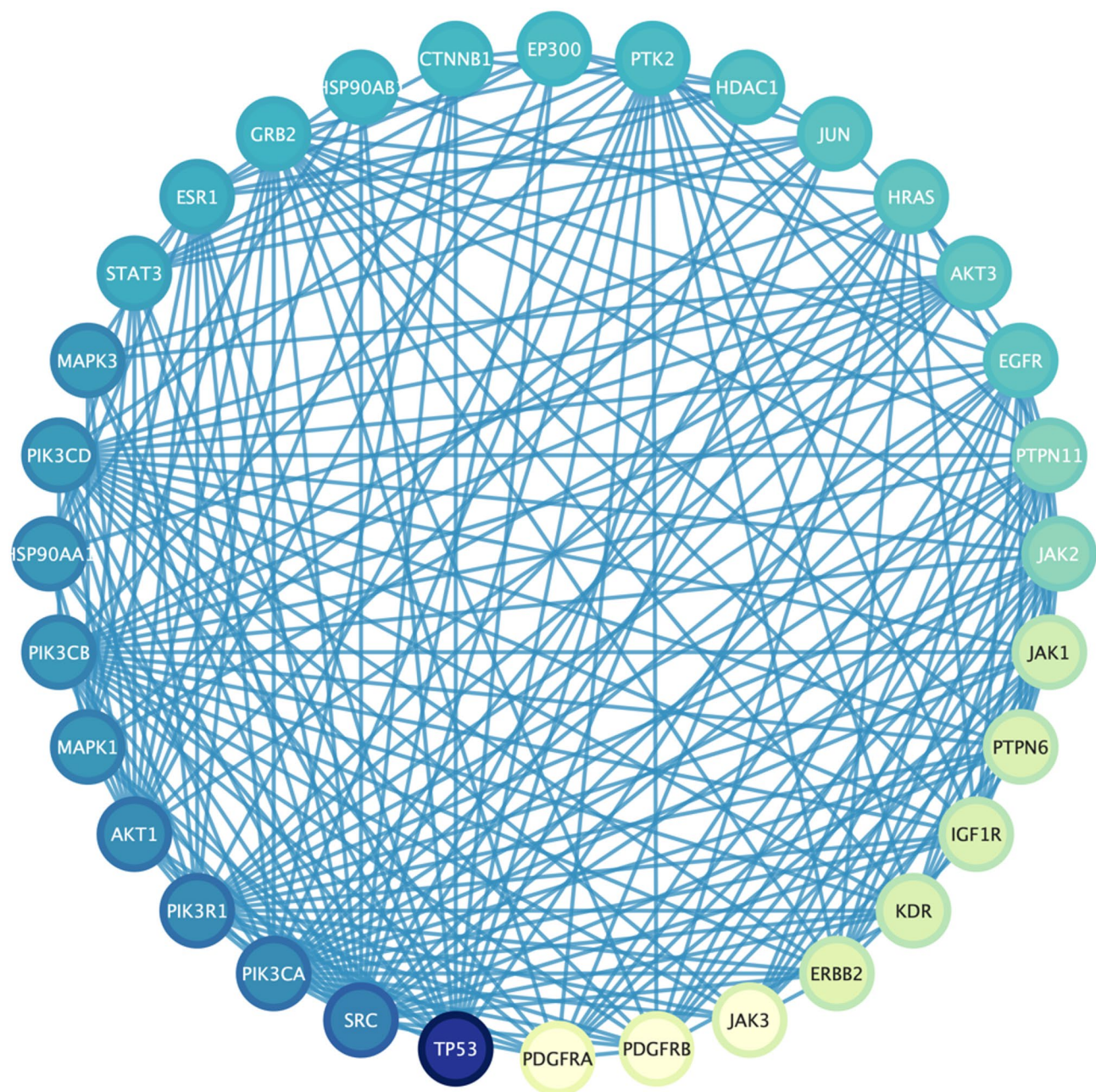
Fig. 3. Network of the top 32 genes identified using MNC and MCC methods, highlighting key interactions among genes associated with cancer, inflammation, and oxidative stress. Central nodes, including TP53, SRC, MAPK1, and AKT1, play crucial roles in cell cycle regulation, signal transduction, and stress responses. This network visualization emphasizes the interconnected roles of these genes and their potential as therapeutic targets of RRM compounds.

tocopherol, kaempferol, raphanin, and beta-ionone—were specifically selected due to their confirmed presence in red radish.

The enrichment analysis revealed key biological processes, molecular functions, and pathways associated with the target genes. Gene Ontology (GO) annotations (Fig. 5A) identified mammary gland epithelium development as the most significantly enriched biological process, while 14-3-3 protein binding was the most enriched molecular function. Additional enriched processes included kinase-related molecular functions, oxidative stress response, cellular stress mechanisms, and telomerase organization, highlighting the potential roles of these targets in cancer, inflammation, and oxidative stress pathways.

The KEGG pathway enrichment analysis (Fig. 5B) ranks pathways based on statistical significance, represented by –log10(p) values and false discovery rates (FDR). Endocrine resistance emerged as the most enriched pathway, exhibiting the lowest FDR and highest –log10(p) value. Other significantly enriched pathways include thyroid hormone signaling, proteoglycans in cancer, and prolactin signaling. Notably, 11 out of the 20

Gene symbol	Full gene name	Betweenness	Closeness	Degree	Stress
TP53	Tumor protein p53	0.16580	0.36032	97	1,575,862
SRC	Proto-oncogene tyrosine-protein kinase	0.05630	0.33269	65	584,680
MAPK1	Mitogen-activated protein kinase 1	0.03301	0.34363	57	446,066
ESR1	Estrogen receptor 1	0.03521	0.34026	47	443,166
AKT1	AKT serine/threonine kinase 1	0.03302	0.34499	60	434,276
MAPK3	Mitogen-activated protein kinase 3	0.02931	0.34119	55	400,168
EP300	E1A binding protein p300	0.04708	0.33946	42	396,576
HSP90AA1	Heat shock protein 90 alpha family class A member 1	0.03881	0.34066	56	374,750
JUN	Jun proto-oncogene	0.03058	0.34444	40	337,184
STAT3	Signal transducer and activator of transcription	0.02892	0.33787	48	327,664
PIK3CA	Phosphatidylinositol-4,5-bisphosphate 3-kinase catalytic subunit alpha	0.01884	0.32473	61	305,404
JAK2	Janus kinase 2	0.01664	0.29020	33	304,780
CTNNB1	Catenin beta-1	0.02517	0.33282	43	248,356
PIK3R1	Phosphoinositide-3-kinase regulatory subunit 1	0.01303	0.31167	61	239,400
HDAC1	Histone deacetylase 1	0.01999	0.31358	41	218,734
PTK2	Protein tyrosine kinase 2	0.01665	0.31912	42	208,326
EGFR	Epidermal growth factor receptor	0.01725	0.32755	39	200,464
HRAS	v-Ha-ras Harvey rat sarcoma viral oncogene homolog	0.01322	0.32256	39	176,010
HSP90AB1	Heat shock protein 90 alpha family class B member 1	0.01459	0.32644	44	173,866
PIK3CB	Phosphatidylinositol-4,5-bisphosphate 3-kinase catalytic subunit beta	0.00815	0.30382	56	173,100
PIK3CD	Phosphatidylinositol-4,5-bisphosphate 3-kinase catalytic subunit delta	0.00776	0.30371	55	168,668
GRB2	Growth factor receptor bound protein 2	0.01752	0.30170	45	158,654
AKT3	AKT serine/threonine kinase 3	0.00697	0.32184	39	143,760
KDR	Kinase insert domain receptor	0.00510	0.29118	23	51,634
ERBB2	Erb-b2 receptor tyrosine kinase 2	0.00153	0.30737	22	42,926
IGF1R	Insulin-like growth factor 1 receptor	0.00271	0.30212	23	41,246
PTPN11	Protein tyrosine phosphatase non-receptor type 11	0.00222	0.29394	34	38,826
PTPN6	Protein tyrosine phosphatase, non-receptor type 6	0.00117	0.28619	23	22,498
JAK1	Janus kinase 1	0.00114	0.27982	24	16,474
JAK3	Janus kinase 3	0.00079	0.27838	18	12,208
PDGFRB	Platelet-derived growth factor receptor beta	0.00013	0.28118	16	3404
PDGFRA	Platelet-derived growth factor receptor alpha	0.00012	0.28100	15	3182

Table 1. Top 32 RRM-targeted proteins associated with cancer, inflammation, and oxidative stress, identified using MNC and MCC methods.

enriched pathways are cancer-related, encompassing specific malignancies such as breast, bladder, prostate, and colorectal cancer. Additionally, key regulatory pathways, including apoptosis and cellular senescence, highlight the involvement of these targets in cancer progression, inflammation, and oxidative stress.

In Silico profiling: drug-likeness, pharmacokinetics, toxicity, and bioactivity predictions

The drug-likeness of the selected compounds was evaluated using Lipinski's Rule of Five, with their physicochemical properties compared against the established criteria (Table 2). Four of the five compounds met the criteria, each presenting fewer than two violations, while kaempferitrin exhibited multiple violations. Specifically, kaempferitrin exceeded the recommended thresholds for molecular weight (> 500 g/mol), hydrogen bond acceptors (> 10), hydrogen bond donors (> 5), and topological polar surface area (TPSA > 140 Å). However, deviations from Lipinski's Rule do not preclude kaempferitrin's potential therapeutic applications.

The pharmacokinetic assessment (Table 3) predicts that all selected compounds exhibit intestinal absorption in humans. Kaempferitrin is unlikely to cross the blood-brain barrier (BBB), likely due to its high molecular weight. Subcellular localization analysis suggests that kaempferitrin, alpha-tocopherol, and kaempferol predominantly localize to the mitochondria, whereas raphanin and beta-ionone are associated with the lysosome. Additionally, none of the compounds are predicted to undergo metabolism via CYP450 2C9 or 2D6, as they are not identified as substrates for these enzymes.

Toxicity classification was assessed using the Globally Harmonized System of Classification and Labelling of Chemicals (GHS), which categorizes compounds into six classes (I–VI) based on predicted LD50 values. Table 4 summarizes the toxicity predictions, identifying two distinct classes among the five compounds. Notably, raphanin is classified as Class III, with a predicted LD50 of 112 mg/kg, suggesting a moderate level of toxicity that warrants further investigation into its safety profile.

Biological activity predictions, as illustrated in Fig. 6, highlight the potential roles of the five key compounds in cancer, inflammation, and oxidative stress regulation. Despite violating Lipinski's rule of five, kaempferitrin
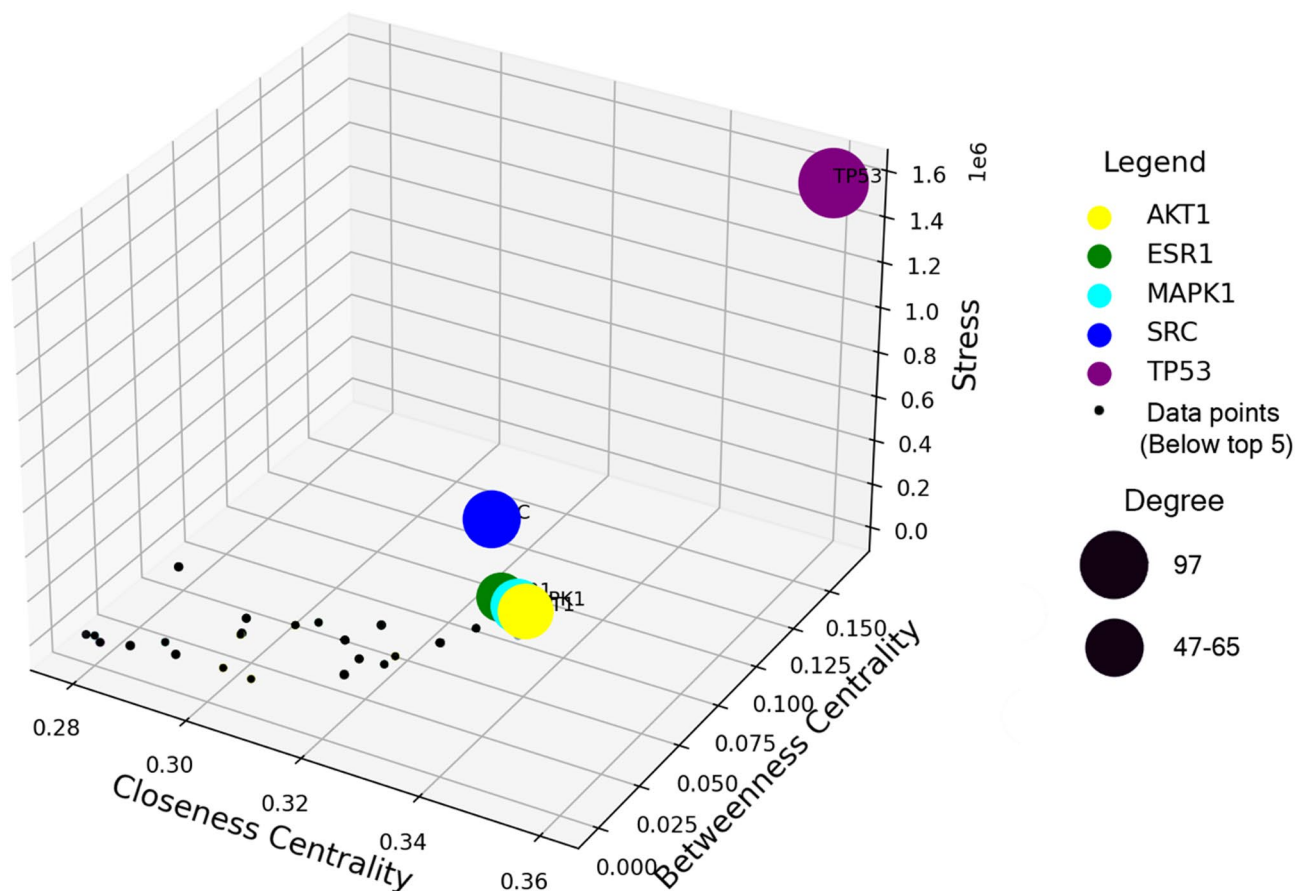
Fig. 4. Skyline results of the top 32 genes based on centrality metrics, highlighting five key genes. The legend indicates the color corresponding to specific genes, while point size represents degree values. Small black dots denote the remaining 27 genes not ranked among the top five.

remains a promising therapeutic candidate, exhibiting a high probability of antioxidant activity (Pa = 0.899), alongside kaempferol (Pa = 0.856). Alpha-tocopherol demonstrates the strongest antioxidant potential with a Pa value of 0.967. Among the compounds, raphanin is associated with the fewest predicted activities, participating in only three. Overall, the five compounds are most likely to exert antioxidant, free radical scavenging, and anti-inflammatory effects, underscoring their potential in mitigating oxidative stress and inflammation.

Molecular Docking and receptor-ligand interaction analysis

The binding affinity analysis (Fig. 7) identifies kaempferitrin as the compound exhibiting the strongest interactions across all five key target proteins. Importantly, its high binding affinity for MAPK1 and SRC underscores its potential role in modulating inflammatory and cancer-related pathways, given the central involvement of these proteins in cell signaling. Furthermore, kaempferitrin's interactions with AKT1 and ESR1, both implicated in cancer progression and oxidative stress, highlight its potential as a multi-target therapeutic agent with antioxidant, anti-inflammatory, and anticancer properties. The calculated binding-free energy (BFE) values range from −9.2 kcal/mol for TP53 to −13.8 kcal/mol for AKT1, further supporting its strong binding capacity to key regulators of oxidative stress, inflammation, and cancer.

Kaempferol, ranking second in binding affinity, also demonstrates substantial potential in modulating inflammation, oxidative stress, and cancer-related pathways, particularly through its interactions with AKT1 and SRC. Although its binding affinities are lower than those of kaempferitrin, its ability to engage these proteins suggests a potential role in exerting antioxidant and anti-inflammatory effects, potentially disrupting cancer cell signaling. In contrast, raphanin exhibited the weakest binding affinity across all target proteins, with significantly lower binding-free energy (BFE) values. This suggests that raphanin may have limited bioactivity in the context of these pathways, particularly when compared to kaempferitrin and kaempferol. Notably, TP53, a central regulator of tumor suppression and cellular stress responses, displayed the lowest binding affinities with all five compounds, indicating that their direct modulation of TP53 may be limited, potentially constraining their anticancer efficacy through this specific pathway.

The receptor-ligand interactions of kaempferitrin with AKT1, ESR1, MAPK1, SRC, and TP53 were analyzed through two-dimensional interaction visualizations (Fig. 8). For AKT1 (Fig. 8A), kaempferitrin demonstrated strong binding through van der Waals forces, hydrogen bonds, and pi interactions, particularly with key residues involved in cancer, inflammation, and oxidative stress regulation. Notably, pi-alkyl and pi-pi stacking
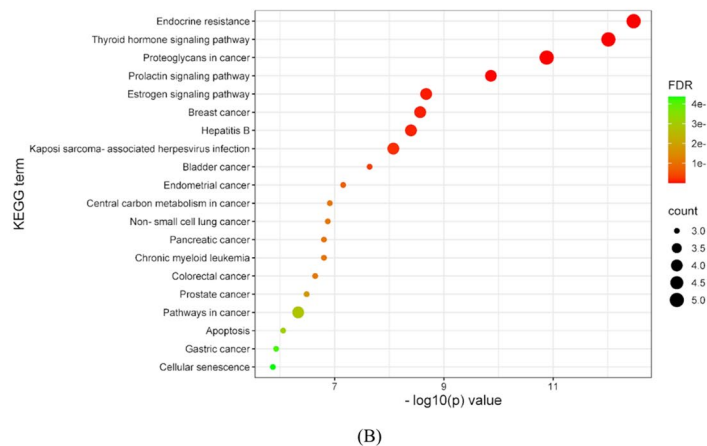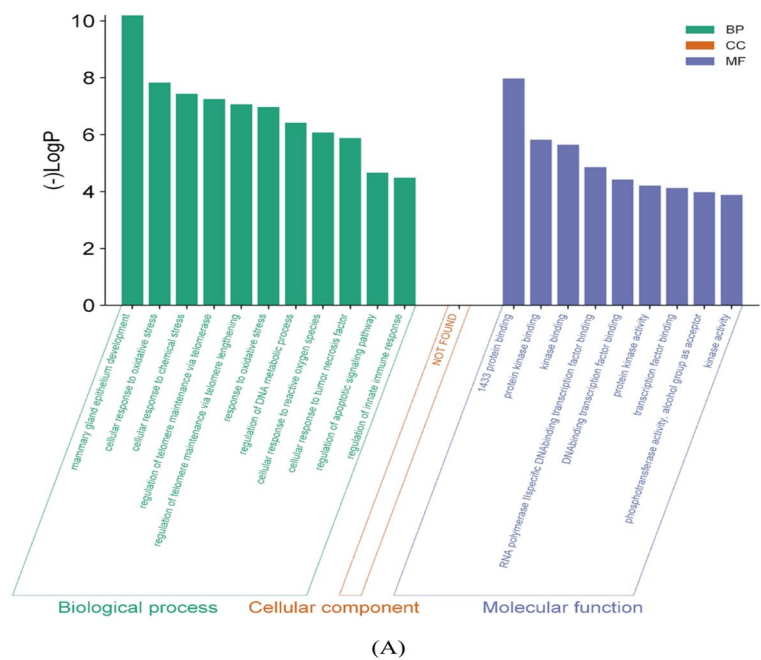
(A)

(B)

Fig. 5. (**A**) Bar plot of Gene Ontology (GO) annotations for the top five genes, illustrating classifications for biological processes and molecular functions. No cellular component annotations were identified for these genes; (**B**) KEGG pathway enrichment analysis of target genes, identifying endocrine resistance as the most significantly enriched pathway. More than half of the enriched pathways are cancer-related, including breast and prostate cancer, alongside key regulatory pathways such as apoptosis and cellular senescence. Dot size represents gene count, while color intensity corresponds to the false discovery rate (FDR), with red indicating the highest significance.

Compound name	Molecular weight (≤ 500 g/mol)	Rotatable bonds (< 10)	Hydrogen bond acceptors (≤ 10)	Hydrogen bond donors (≤ 5)	Topological polar surface area (≤ 140Å)	Violation (< 2) (AdmetLAB)	Lipinski's rule of five
Kaempferitrin	578.16	5	13	8	228.97	4	Rejected
Alpha-Tocopherol	430.38	12	2	1	29.46	1	Accepted
Kaempferol	286.05	1	5	4	111.13	0	Accepted
Raphanin	175.01	4	3	0	35.42	0	Accepted
Beta-Ionone	192.15	2	1	0	17.07	0	Accepted

Table 2. Drug-likeness characteristics of the compounds evaluated based on Lipinski's rule of five (Ro5) properties, with additional predictions derived from admetlab and ProTox analyses.

Compound name	Human intestinal absorption	BBB permeability	Subcellular localization	CYP450 2C9 substrate	CYP450 2D6 substrate
Kaempferitrin	+	−	Mitochondria	No	No
Alpha-Tocopherol	+	+	Mitochondria	No	No
Kaempferol	+	+	Mitochondria	No	No
Raphanin	+	+	Lysosome	No	No
Beta-Ionone	+	+	Lysosome	No	No

Table 3. Predicted absorption, distribution, metabolism, and excretion (ADME) properties of the five principal compounds. A "+" indicates a positive likelihood, while a "−" denotes a negative likelihood.

Compound name	ProTox 3 toxicity predictions		
	Predicted toxicity class	Predicted LD$_{50}$	Hepatoxicity
Kaempferitrin	V	5000 mg/kg	No
Alpha-Tocopherol	V	5000 mg/kg	No
Kaempferol	V	3919 mg/kg	No
Raphanin	III	112 mg/kg	No
Beta-Ionone	V	4590 mg/kg	No

Table 4. Toxicity predictions for the five principal compounds, including predicted toxicity class, LD50 values, and hepatotoxicity assessments.

interactions within hydrophobic regions, as well as a pi-anion interaction with ASP292, contributed to the stability of the complex. However, an unfavorable donor-donor interaction with ARG200 suggests a potential structural constraint, highlighting an opportunity for molecular optimization to enhance binding affinity and minimize steric hindrance.

Kaempferitrin's interaction with ESR1 (Fig. 8B) was characterized by van der Waals forces with 12 residues and hydrogen bonding with THR347, MET343, and LEU387, along with multiple pi interactions. The van der Waals forces facilitated an optimal fit within ESR1's hydrophobic binding site, while hydrogen bonding with polar residues contributed to complex stability and specificity. These interactions are crucial for ESR1 modulation in cancer progression, despite an unfavorable donor-donor interaction with ARG394.

For MAPK1 (Fig. 8C), Kaempferitrin formed a stable complex through a combination of van der Waals forces, hydrogen bonding with MET108, THR110, and ASP167, and pi interactions, including pi-cation and pi-alkyl contacts. The pi-cation interactions stabilized the complex by attracting charged residues within the binding pocket, enhancing ligand affinity. While an unfavorable donor-donor interaction with ARG67 was noted, the overall binding profile suggests that kaempferitrin holds potential as a modulator of MAPK1 in inflammation and cancer pathways.

In the SRC complex (Fig. 8D), kaempferitrin established strong interactions through van der Waals forces, hydrogen bonds, and pi interactions. While unfavorable contacts with ASP404 and MET341 suggest potential areas for structural refinement, the overall binding profile supports its role in modulating SRC-related pathways in cancer and cell signaling. The hydrogen bonds in this complex enhance binding specificity, ensuring a stable ligand-protein interaction conducive to SRC regulation.

Kaempferitrin's binding to TP53 (Fig. 8E) involved multiple van der Waals forces, hydrogen bonds, and pi-alkyl and pi-pi stacking interactions, highlighting its potential role in modulating this key tumor suppressor. The pi-alkyl interactions contributed to binding stability within TP53's hydrophobic pocket, while pi-pi stacking further reinforced ligand affinity, suggesting a potential therapeutic application in cancer treatment.

In Fig. 8A-D, unfavorable donor-donor interactions were noted; however, these are effectively counterbalanced by strong interactions, including conventional hydrogen bonds and pi-pi stacking. Additionally, the collective presence of van der Waals forces, hydrogen bonds, and pi interactions across all five protein complexes underscores the overall binding stability, thereby supporting kaempferitrin's potential as a multi-target modulator in therapeutic applications for cancer, inflammation, and oxidative stress.

Molecular dynamics simulations analysis

The AKT1-kaempferitrin complex was selected for molecular dynamics simulations due to its excellent interaction, as shown by molecular docking results. AKT1 is a crucial serine/threonine kinase that regulates cell survival, growth, and metabolism, making it an important target in studies of inflammation, oxidative stress, and cancer. Furthermore, dysregulation of AKT1 is linked to heightened inflammatory responses, weakened antioxidant defenses, and uncontrolled cell proliferation, all of which are central to these disease processes.

Figure 9A shows the simulation contrasting protein and ligand RMSD over 100 ns. Initially, AKT1 RMSD increases steadily as the structure undergoes adjustments but later stabilizes around 4.0 Å after approximately 20 ns, indicating that the protein achieves equilibrium and remains structurally stable throughout the remainder of the simulation. In contrast, kaempferitrin RMSD exhibits significant fluctuations, suggesting that its binding
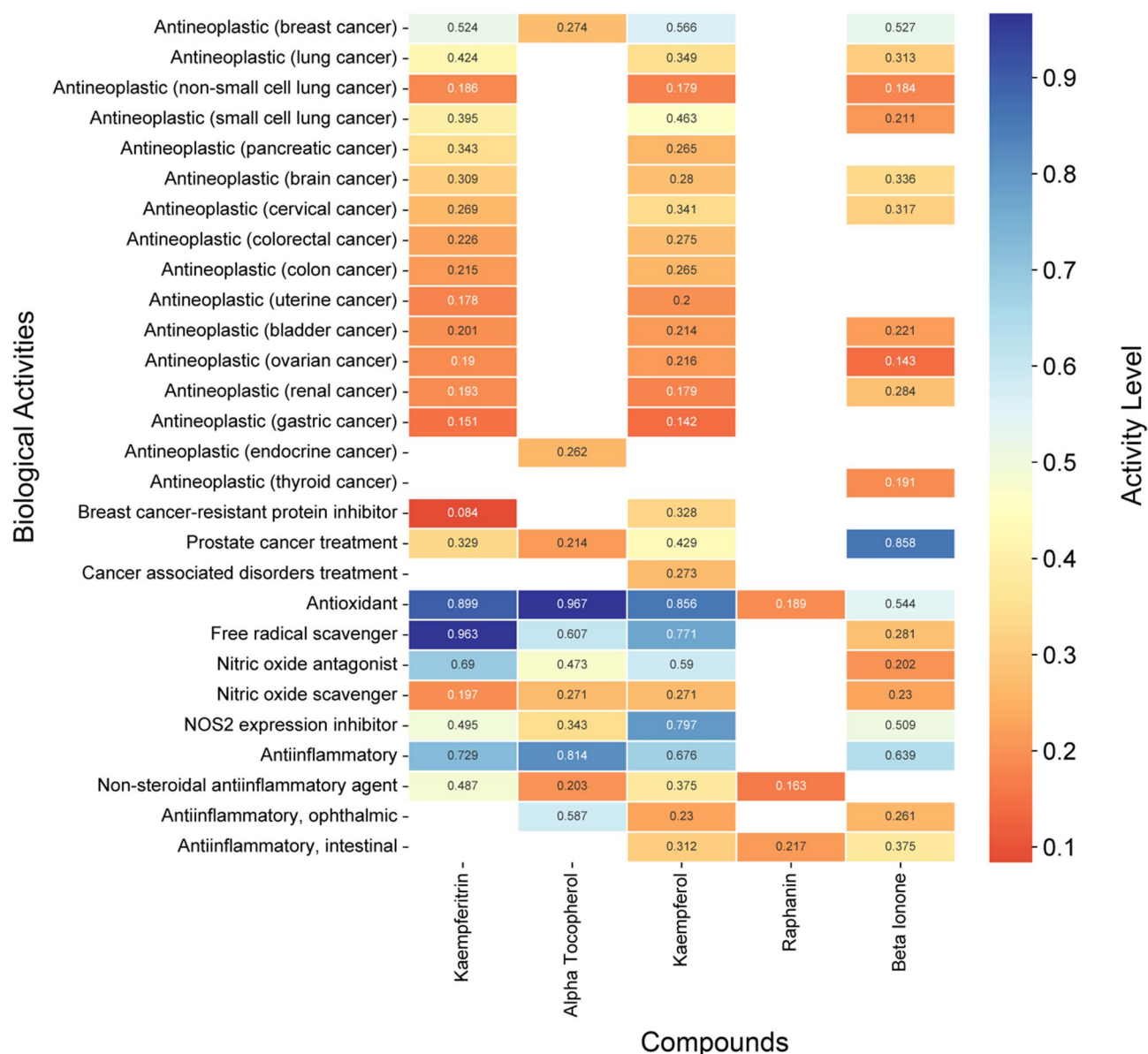
Fig. 6. Predicted biological activities of the five key compounds, focusing on their roles in cancer, inflammation, and oxidative stress. Pa values indicate the probability of bioactivity, with values above 0.7 suggesting strong potential for laboratory validation, values between 0.5 and 0.7 indicating moderate activity with expected in vivo and in vitro relevance, and values below 0.5 requiring further experimental confirmation.

position is dynamic and possibly unstable. This behavior implies that the ligand might be adopting multiple conformations within the binding site.

Figure 9B illustrates the RMSF profile of AKT1, revealing distinct regions of flexibility and stability throughout the simulation. The plot indicates that residues 100–120 exhibit relatively high fluctuations (approximately 5.6 Å), suggesting considerable dynamic movement in this region, which likely corresponds to parts of the N-terminal region adjacent to the PH domain. In contrast, residues 150–408, which constitute the kinase domain essential for AKT1's catalytic activity, display lower fluctuations (around 0.8 Å), reflecting the structural stability required for enzymatic function. Additionally, the C-terminal region, particularly near residue 450 where fluctuations reach about 6.8 Å, indicates increased mobility that may be related to regulatory processes. The green-highlighted residues, which engage with the ligand, further emphasize the functional relevance of these domains by illustrating specific interaction sites within these regions.

The kaempferitrin RMSF (Fig. 9C) shows that its core atoms have minimal fluctuations, indicating a stable conformation within the protein's active site. In contrast, some regions—likely the flexible terminal groups or side chains—exhibit greater fluctuations, suggesting subtle dynamic adjustments for optimal binding. Overall, while the ligand maintains a stable binding mode, localized flexibility is essential for fine-tuning its interactions with the protein.
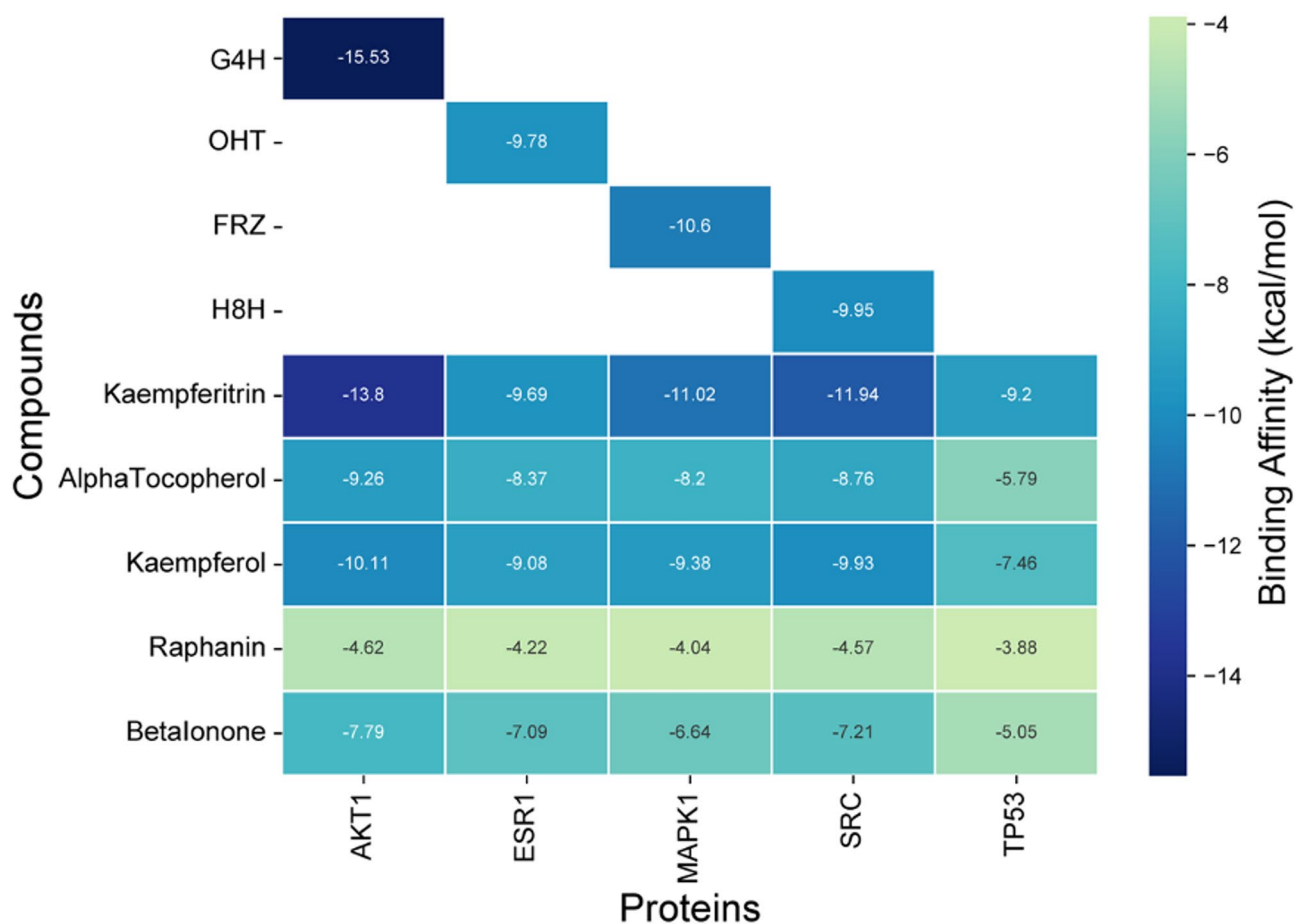
Fig. 7. Docking analysis of the five key proteins, demonstrating the binding affinities of the most prominent complexes redocked with the native ligand (GH4, OHT, FRZ, H8H) and the five principal compounds under investigation.

Figure 9D shows that the interaction contacts between AKT1 and kaempferitrin reveal stable engagement of key residues, with high interaction fractions observed for GLN-79 and TRP-80 in the PH domain and LYS-268, TYR-272, ASP-292, and GLY-294 in the kinase domain. Additionally, significant hydrophobic interactions are noted at residues LYS-179, LEU-264, and VAL-270. The binding is mediated by a combination of hydrogen bonds, hydrophobic interactions, water-mediated interactions, and some ionic interactions, with hydrogen bonds being especially prominent at GLN-79, ASP-292, and GLY-294 and hydrophobic interactions notably observed at TRP-80, LYS-179, LEU-264, VAL-270, and TYR-272. The clustering of these interacting residues suggests a defined binding site at the interface of the PH and kinase domains, which enhances the overall stability of the complex.

The AKT1's radius of gyration remains relatively constant throughout the simulation, indicating that its overall compactness is maintained (Fig. 9E). Although minor fluctuations are evident, these only suggest small conformational adjustments without any indication of unfolding or major structural rearrangements. This stability in the radius of gyration confirms that the protein structure is well-maintained under the simulated conditions. The SASA (solvent accessible surface area) analysis reveals a relatively stable profile throughout the simulation period (Fig. 9F). The plot shows minor fluctuations around a consistent mean value, indicating that the protein maintains its overall surface exposure to solvent without undergoing significant conformational changes that would alter its interaction with the surrounding environment. This stability in SASA values suggests that the protein-ligand complex preserves its structural integrity, with no major unfolding events or substantial rearrangements of surface-exposed regions. The consistent SASA profile further supports that the binding of the ligand does not induce dramatic alterations in the protein's surface topology, suggesting a well-accommodated binding mode that maintains the native-like characteristics of the protein structure.

The GROMACS energy shows that the total energy remains stable over the simulation (Fig. 9G). The potential energy is computed using a designated force field that accounts for van der Waals, electrostatic, and bonded interactions (bond, angle, and dihedral energies). The energy plot for the AKT1-kaempferitrin interaction, reveals significant fluctuations that remain confined to a narrow range of approximately -5.26×10^5 and -5.36×10^5 kJ/mol. The absence of any discernible trend indicates that the system has reached equilibrium and is not undergoing major structural changes. The random oscillations around a consistent average and the high negative energy values further confirm that the interaction between AKT1 and kaempferitrin is energetically favorable and stable.
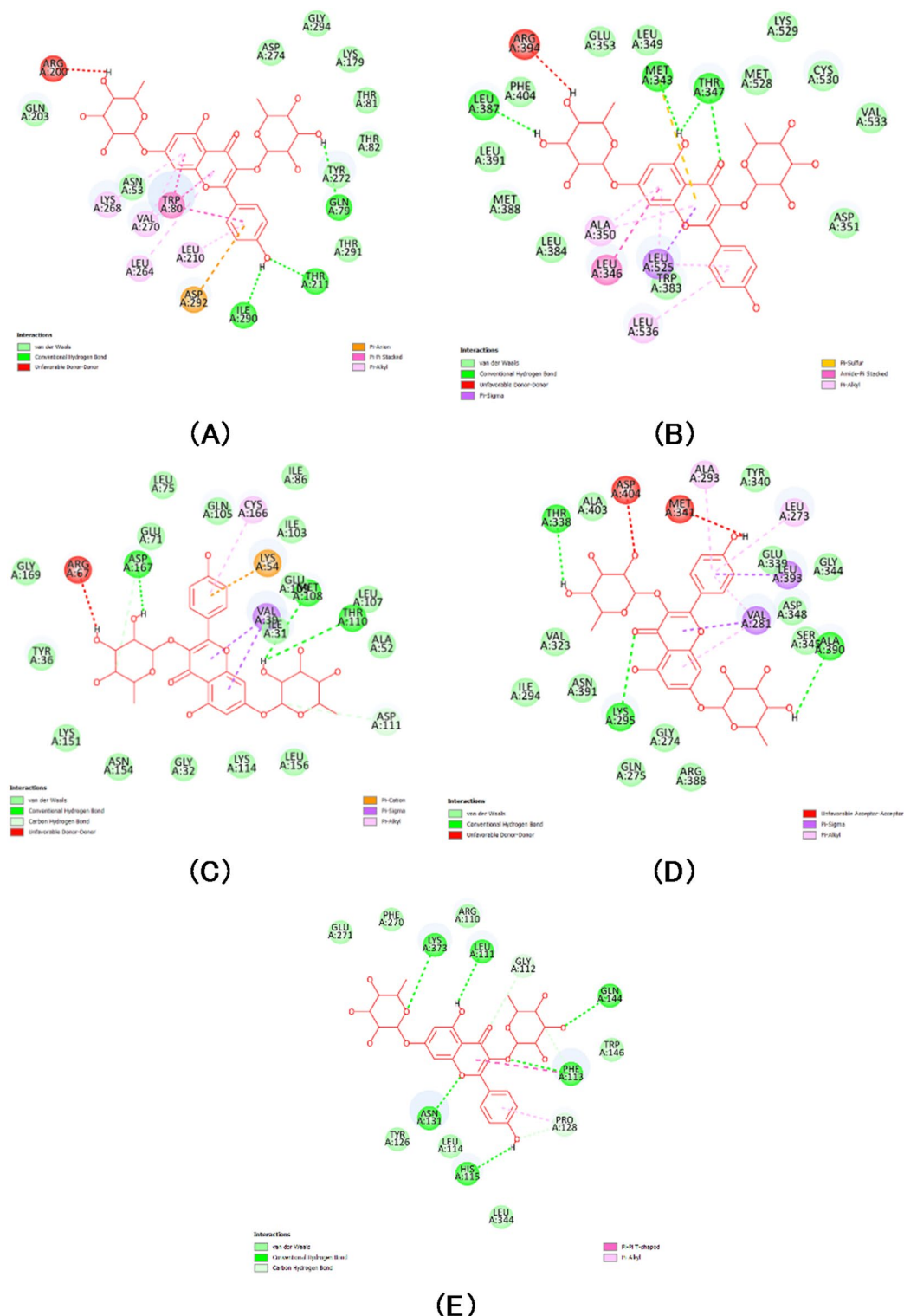
Fig. 8. Two-dimensional representation of the interactions between kaempferitrin and key proteins: (**A**) AKT1-kaempferitrin interaction, (**B**) ESR1-kaempferitrin complex, (**C**) MAPK1-kaempferitrin interaction, (**D**) SRC-kaempferitrin complex, and (**E**) TP53-kaempferitrin interaction.

These MD simulations reveal that the AKT1-kaempferitrin complex exhibits a dynamic binding mode, with the ligand undergoing significant fluctuations, yet the protein–ligand interface remains stable due to persistent hydrogen bonds, hydrophobic interactions, and water-mediated bridges. The stable protein structure—evidenced by consistent radius of gyration, SASA, and energy profiles—demonstrates that its overall conformation is maintained throughout the simulation. These insights are critical for drug design, as they identify potential

(A)

(B)

(C)

(D)

(E)

(F)

(G)
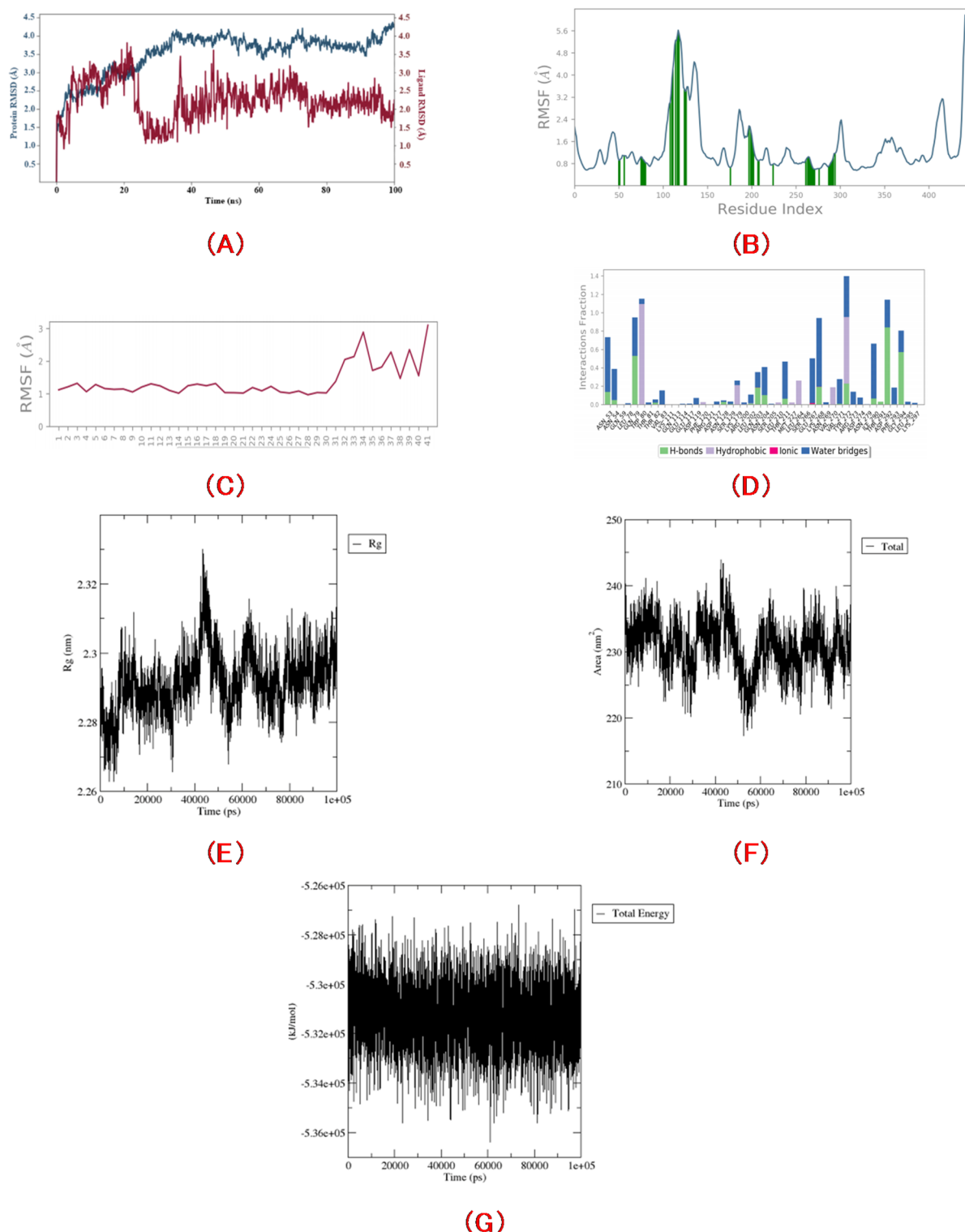
binding hotspots for developing potent and selective AKT1 inhibitors and deepen our understanding of AKT1's role in essential cellular processes and diseases.

In vivo evaluation of RRM extract: toxicity, survival, immune modulation, and oxidative stress regulation in Dm *PGRP-LB$^\Delta$* mutants

A toxicity assay was conducted to assess the effects of RRM extract on the survival and developmental progression of *Drosophila melanogaster* (Dm) *PGRP-LB$^\Delta$* mutants (Fig. 10A). The proportion of larvae reaching the pupal stage was evaluated under untreated control conditions, ethanol (70%) treatment, and RRM extract exposure at concentrations of 1.25%, 0.625%, and 0.312%. No statistically significant differences were observed among the treatment groups, suggesting that RRM extract did not adversely impact larval-to-pupal development. Similarly, the pupal-to-adult transition rates (Fig. 10B) remained unaffected across treatments, with no significant

Fig. 9. Molecular dynamics simulation of AKT1 and kaempferitrin complex. (**A**) RMSD plot over 100 ns comparing protein and ligand. The protein RMSD rises and stabilizes around 4.0 Å after ~ 20 ns, indicating equilibrium and stability, while the ligand RMSD fluctuates, suggesting dynamic binding or weak affinity. (**B**) The RMSF profile of AKT1 reveals high flexibility in residues 100–120 (~ 5.6 Å) adjacent to the PH domain and near residue 450 (~ 6.8 Å) in the C-terminal region, while the kinase domain (residues 150–408) exhibits low fluctuations (~ 0.8 Å) indicative of structural stability. Green-highlighted residues denote ligand interaction sites. (**C**) Ligand RMSF reveals low fluctuations for core atoms, indicating stable binding, with higher fluctuations in flexible regions, suggesting dynamic adjustments for optimal protein interactions. (**D**) The interaction contacts between AKT1 and kaempferitrin reveal stable binding via key residues: GLN-79 and TRP-80 in the PH domain, and LYS-268, TYR-272, ASP-292, and GLY-294 in the kinase domain, with additional hydrophobic interactions at LYS-179, LEU-264, and VAL-270. These findings suggest a defined binding site at the interface of the PH and kinase domains. (**E**) The radius of gyration remains stable throughout the simulation, with only minor fluctuations indicating small conformational adjustments, confirming that the protein maintains its overall compactness and structural integrity. (**F**) The SASA shows a stable solvent-accessible surface area with only minor fluctuations, indicating that the protein-ligand complex maintains its native-like structure without significant conformational changes. (**G**) The GROMACS energy analysis shows that the total energy of the AKT1-kaempferitrin complex remains stable, fluctuating narrowly between -5.26×10^5 and -5.36×10^5 kJ/mol, indicating an equilibrated and energetically favorable system.
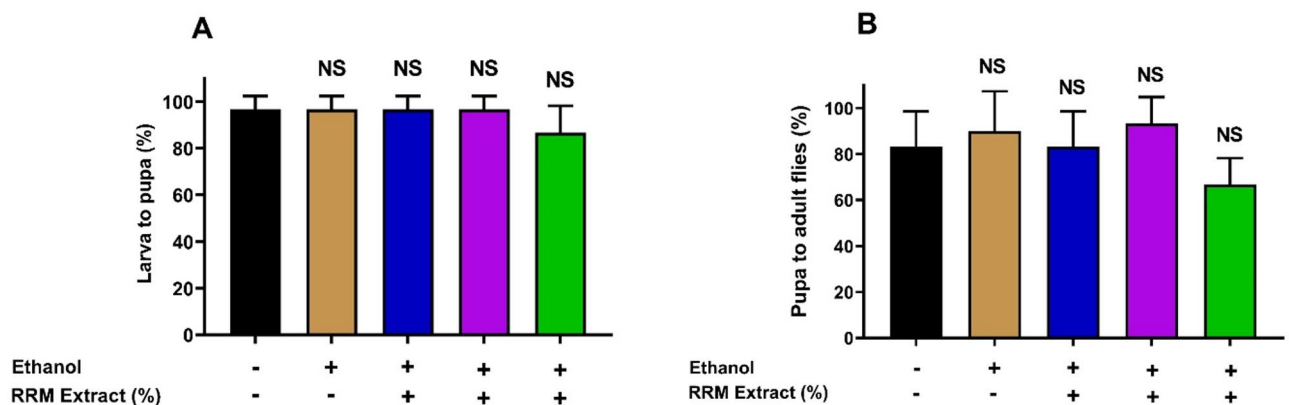

Fig. 10. RRM extract is non-toxic at concentrations of 1.25%, 0.625%, and 0.312% in Dm *PGPR-LB$^\Delta$*. (**A**) Survival rate from larva to pupa, (**B**) Survival rate from pupa to adult. NS indicates no statistically significant difference. Symbols: '−' = treatment not applied; '+' = treatment applied.

reduction in adult emergence even at the lowest concentration (0.312%), despite a slight decrease in the average conversion rate in this group. These findings indicate that RRM extract does not exert overt toxicity on Dm *PGRP-LB$^\Delta$* at the tested concentrations.

The results presented in Fig. 11 demonstrate that RRM extract significantly enhances the survival of *PGRP-LB$^\Delta$* larvae in a dose-dependent manner. The untreated control group maintained a near-100% survival rate, whereas larvae exposed to heat-killed *E. coli* (HKE) exhibited a substantial decline in survival, indicating the detrimental effect of HKE. Treatment with 70% ethanol showed no significant difference in survival compared to the HKE-exposed group. Larvae treated with 2.5% RRM extract showed lower survival rates, comparable to or even below those receiving HKE alone. In contrast, lower RRM concentrations (1.25%, 0.625%, and 0.312%) significantly restored survival to near-control levels, with statistical significance at $p < 0.001$ and $p < 0.0001$, indicating a beneficial effect at these doses. These findings highlight an inverse dose-response relationship where lower extract concentrations provide better protective effects in mitigating HKE-induced lethality in *PGRP-LB$^\Delta$* larvae.

Figure 12. Exposure to HKE induces the expression of immune system genes in Dm *PGRP-LB$^\Delta$* larvae. Administration of RRM extract at concentrations of 1.25%, 0.625%, and 0.312% resulted in a decrease in the expression of the *dptA* (**A**) and *totA* (**B**) genes at all concentrations. NS indicates non-significant differences; ***$p < 0.001$; and ****$p < 0.0001$. Symbols: '−' = treatment not applied; '+' = treatment applied.

HKE treatment significantly increased reactive oxygen species (ROS) levels in larvae, indicating oxidative stress as part of the immune response. Administration of RRM extract at a concentration of 1.25% further elevated ROS levels, whereas treatment with 0.625% and 0.312% led to a significant reduction (Fig. 13). The increase observed at 1.25% was likely due to the presence of bioactive compounds in the extract that enhanced oxygen reactivity, thereby promoting oxidative stress. In contrast, at 0.625% and 0.312%, the extract appeared to provide sufficient antioxidant capacity to neutralize ROS, mitigating oxidative stress and lowering ROS levels.

The increased oxidative stress at 1.25% RRM extract treatment was further reflected in the upregulation of *sod1* gene expression (Fig. 13A and **B**). This suggests that cells responded to oxidative stress by upregulating superoxide dismutase 1 (SOD1), a key enzyme that catalyzes the conversion of superoxide radicals into hydrogen
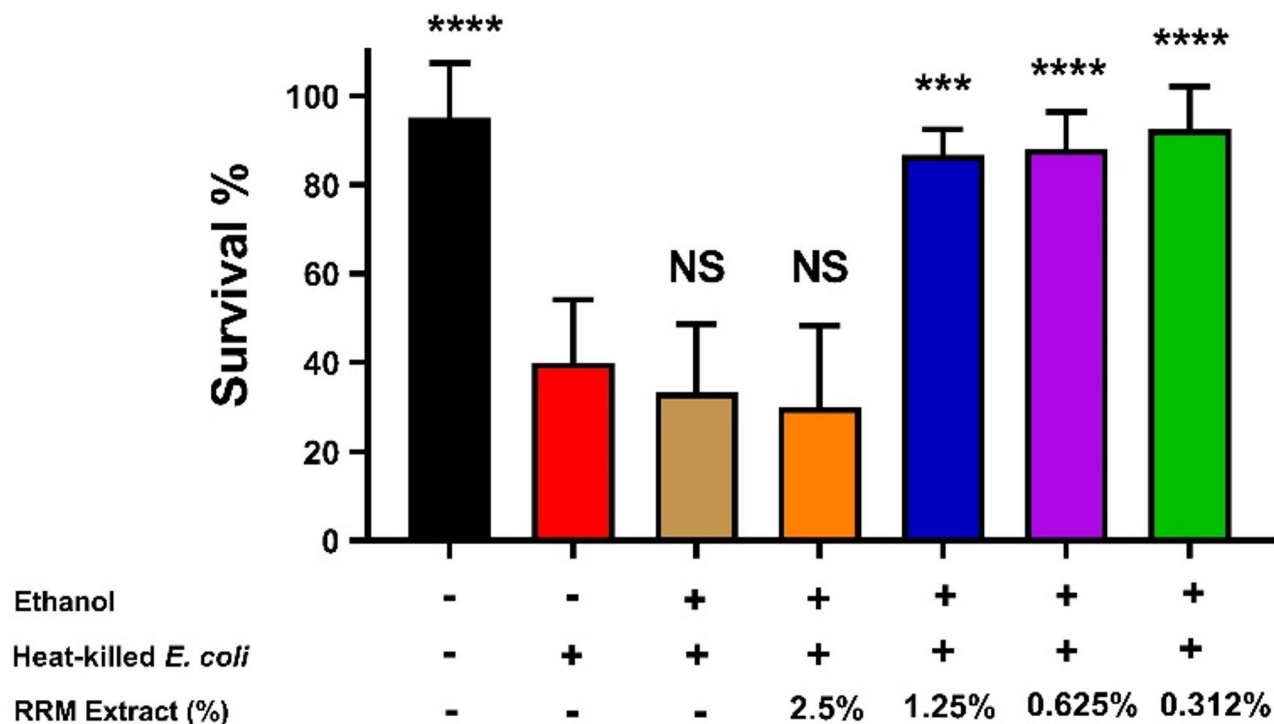
Fig. 11. Dm *PGRP-LB$^{\Delta}$* larvae showed reduced survival when treated with a 2.5% RRM extract, whereas treatments at 1.25%, 0.625%, and 0.312% enhanced survival. NS indicates non-significant differences; ***$p < 0.001$; and ****$p < 0.0001$. Each treatment was compared to heat-killed *E. coli* as the control. Symbols: '–' = treatment not applied; '+' = treatment applied.
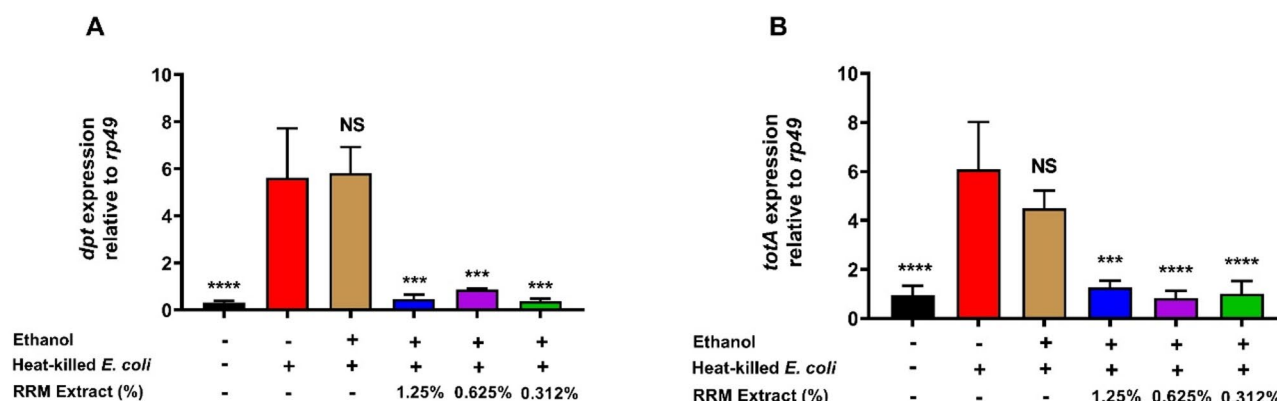

Fig. 12. demonstrates that exposure to HKE markedly upregulates the expression of the *dptA* and *totA* genes. In contrast, treatment with RRM extract at concentrations of 1.25%, 0.625%, and 0.312% significantly suppresses the expression of both genes. These findings suggest that in Dm *PGRP-LB$^{\Delta}$*, RRM extract modulates immune responses, potentially mitigating the detrimental effects of excessive immune activation.

peroxide (H_2O_2), which is subsequently broken down by catalase. Notably, the enhanced *sod1* expression correlated with a reduction in *totA* expression, which has been linked to ROS-driven cellular proliferation. In contrast, the expression levels of *sod2* and *cat* genes, which encode SOD2 and catalase, respectively, were significantly downregulated following RRM extract treatment (Fig. 13C and **D**). This downregulation, combined with the increased ROS levels observed at 1.25% extract concentration, suggests a potential reduction in internal antioxidant capacity. The impaired expression of these enzymes may have limited the conversion of H_2O_2 into water and oxygen, thereby exacerbating oxidative stress. These findings indicate that while RRM extract at lower concentrations (0.625% and 0.312%) exerted an antioxidant effect by reducing ROS levels, a higher concentration (1.25%) paradoxically induced oxidative stress, possibly through bioactive compounds that modulate redox homeostasis.
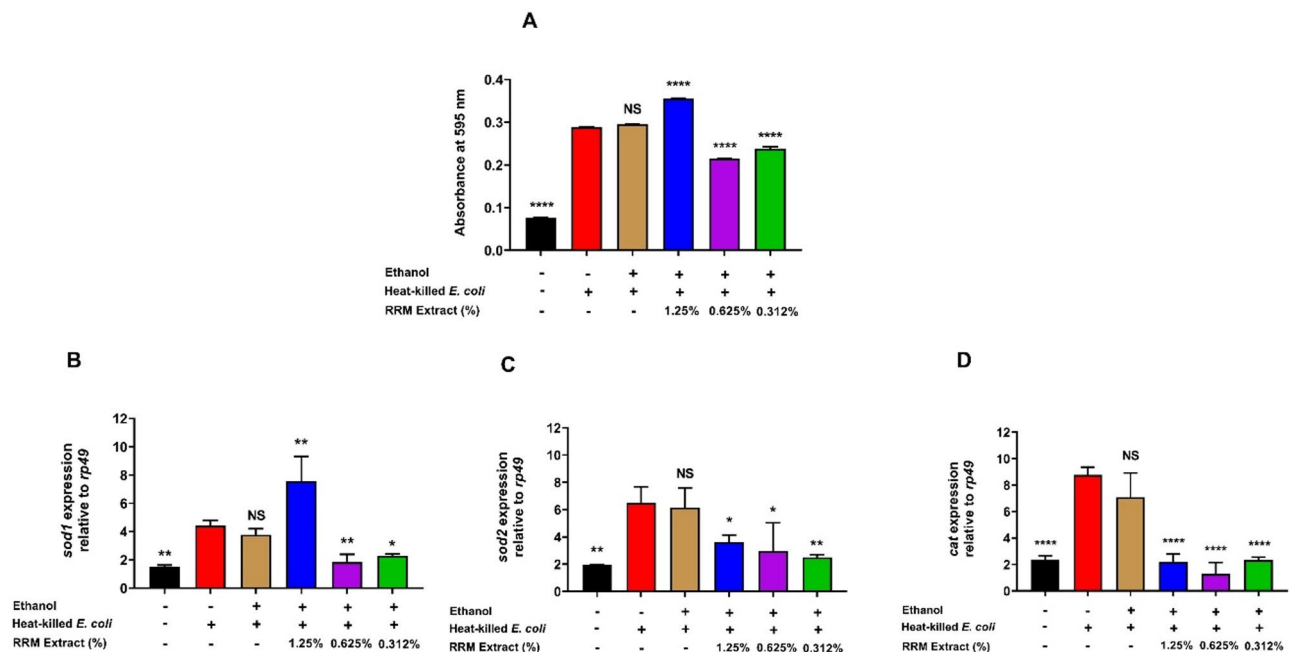
Fig. 13. RRM extract modulates ROS and antioxidant activity. Increased ROS (**A**): Treatment with HKE elevated ROS levels in Dm *PGRP-LB$^\Delta$* larvae, while administration of extracts at concentrations of 0.625% and 0.312% resulted in a reduction in ROS levels. Increased *sod1* gene expression (**B**): At a concentration of 1.25%, RRM extract led to increased expression of the *sod1* gene, accompanied by decreased expression of the *sod2* (**C**) and *cat* (**D**) genes. NS indicates non-significant differences; ***$p < 0.001$; **$p < 0.01$; *$p < 0.05$. Symbols: '–' = treatment not applied; '+' = treatment applied.

Discussion

Species in the Brassicaceae family are rich in bioactive phytochemicals, including glucosinolates, isothiocyanates, phenolic compounds, carotenoids, tocopherols, and ascorbic acid[23,24]. These compounds have been extensively studied for their roles in modulating inflammation, oxidative stress, and cancer-related pathways. Isothiocyanates (ITCs), with their reactive $-N=C=S$ group, exhibit potent anticancer, anti-inflammatory, and antioxidant properties[25,26]. Understanding the molecular mechanisms underlying these effects requires a network-based approach to identify key regulatory proteins.

Metabolic profiling of RRM extract confirmed a diverse composition of bioactive molecules, suggesting therapeutic potential. Phenolic compounds, including flavonoids and glucosinolates, act as free radical scavengers, reducing oxidative stress and inflammation. Sulfur-containing heterocyclic compounds, characteristic of cruciferous vegetables, support detoxification and may contribute to anticancer activity. Additionally, lipids and fatty acyls, upon metabolism, generate bioactive lipid mediators that regulate immune function and oxidative stress. Amino acids and their derivatives contribute to metabolic homeostasis and enhance bioavailability of other bioactive compounds. The presence of vitamins, terpenes, and alkaloids further strengthens the extract's antioxidant and anti-inflammatory profile.

Network pharmacology facilitates the identification of these regulatory proteins through centrality measures and degree distribution. Centrality metrics play a crucial role in determining key nodes within a network: degree centrality identifies hubs based on their connectivity, betweenness centrality highlights bridging nodes that mediate communication between clusters, closeness centrality measures connectivity efficiency, and stress centrality quantifies the burden placed on nodes by the shortest paths. In Cytoscape, stress centrality serves as a topological metric to assess a node's influence on network flow, increasing proportionally with the number of shortest paths passing through it[27,28]. Collectively, these metrics provide critical insights into the functional significance of proteins in complex biological systems[29–31].

The integrated network and centrality rankings identify TP53 as the most central node, reinforcing its crucial role in cancer and oxidative stress pathways. Consistent with this, previous research has established TP53 as a key mediator of cellular stress responses and a major contributor to cancer development and progression[32]. Other highly ranked proteins, including SRC, MAPK1, ESR1, and AKT1, demonstrated significant contributions across centrality measures, emphasizing their importance in signaling pathways associated with inflammation and cancer[33–36].

Among the 32 RRM-targeted proteins associated with cancer, inflammation, and oxidative stress, STAT3, JAK2, and PIK3CA emerged as critical regulators of cell proliferation and immune responses. The JAK2/STAT3 signaling pathway plays a fundamental role in cytogenesis and is closely linked to osteoarthritis (OA) progression[37]. Additionally, PIK3CA contributes to tumor progression and immune infiltration by mediating interactions between CD8$^+$ T cells and macrophages[38].

The presence of MAPK1, MAPK3, and JUN among the RRM-targeted proteins underscores the significance of MAPK signaling in oxidative stress and inflammation. The MAPK family, including extracellular signal-regulated kinases (ERKs), c-Jun N-terminal kinases (JNKs), and p38 MAPKs, mediates extracellular signal transmission to the nucleus, regulating gene expression. Among these, ERK1/2, JNKs, and p38 MAPKs play pivotal roles in modulating inflammatory responses[39,40].

Additionally, the identification of heat shock proteins HSP90AA1 and HSP90AB1 highlights the importance of stress response mechanisms and protein folding in maintaining cellular stability during oxidative stress[41]. Growth factor-related proteins such as EGFR, ERBB2, and PTPN11, along with kinases including PIK3R1, PIK3CB, and PIK3CD, further emphasize the role of the PI3K/AKT and receptor tyrosine kinase pathways in cancer progression and cellular adaptation under oxidative and inflammatory stress conditions[42–44].

While lower-ranked proteins such as JAK1, JAK3, PDGFRB, and PDGFRA remain relevant in specific regulatory pathways[45,46]. the diversity of these 32 proteins highlights the extensive impact of RRM compounds on interconnected pathways involved in cancer, inflammation, and oxidative stress. Key targets include transcription factors (TP53, JUN, STAT3), kinases (SRC, AKT1, MAPK1), and stress-response proteins (HSP90AA1), which collectively contribute to the molecular mechanisms influenced by RRM compounds.

Given the complex interplay among signaling networks, the pharmacodynamic interactions of RRM compounds warrant further investigation. Certain compounds may act synergistically by engaging complementary nodes in pathways such as PI3K/AKT and JAK/STAT, which are critical for regulating cellular transitions and intracellular signal transduction[47,48]. Conversely, antagonistic effects may occur if compounds exert opposing influences on shared signaling molecules, potentially diminishing their overall impact[49]. Previous studies suggest that multi-targeted therapies can either enhance or impair treatment responses depending on the molecular context and pathway crosstalk[50].

Specifically, modulation of the JAK/STAT pathway by RRM extract may occur via multiple mechanisms. One possibility is direct receptor inhibition, whereby bioactive compounds interfere with cytokine binding to their receptors, preventing subsequent activation of Janus kinases (JAKs) and phosphorylation of STAT proteins[51]. Alternatively, the extract might influence the JAK/STAT pathway indirectly through its antioxidant properties. By neutralizing ROS, which function as secondary messengers and enhance inflammatory signaling, the extract can lower oxidative stress and prevent excessive activation of the pathway[52]. Moreover, the extract may also affect the expression of inhibitory regulators such as suppressor of cytokine signaling (SOCS) proteins, thereby further contributing to the downregulation of JAK/STAT signaling[53].

A deeper understanding of these combinatorial effects will provide valuable insights for optimizing RRM compounds as co-therapeutic agents, as well as for identifying potential counteractive interactions that may limit efficacy. These findings lay a foundation for further experimental validation to fully elucidate the therapeutic potential of RRM compounds in modulating these critical pathways.

The key compounds in RRM that target the aforementioned proteins include kaempferitrin, alpha-tocopherol, kaempferol, raphanin, and beta-ionone, all of which have been previously reported in radish[54–58]. Notably, radish microgreens exhibit significantly higher concentrations of nutrients than their mature counterparts, containing 2–4 times more ascorbic acid, 4.5 times more carotenoids, 4–5 times more isothiocyanates, and an astounding 976 times more α-tocopherol[59]. To further elucidate protein interactions, skyline queries—used to select a subset of optimal data points based on multiple criteria—were conducted using the network topology and centrality measures of the top 32 proteins. This approach, with a particular emphasis on stress centrality, identified the five most essential proteins within the network[60].

Pharmacokinetic and drug-likeness evaluations provided insights into the potential efficacy and metabolic processing of the five principal compounds[61,62]. Although kaempferitrin does not fully comply with Lipinski's Rule of Five—a guideline primarily applicable to small synthetic molecules—it remains a promising therapeutic candidate, as many natural compounds, peptides, and larger bioactive molecules (such as flavonoids and antibiotics) are effective despite such violations[63]. Toxicity assessments classified four of the compounds as Class V (with predicted LD50 values of 2000–5000 mg/kg), while raphanin is the only compound in toxicity Class III (LD50 of 112 mg/kg), underscoring the need for further safety evaluation[64,65].

In terms of bioavailability, these compounds differ due to variations in structure, solubility, and metabolic processing. For example, kaempferitrin, a flavonoid glycoside, must be hydrolyzed to release its aglycone, kaempferol, which is then rapidly conjugated in the liver, contributing to its limited bioavailability[66]. In contrast, alpha-tocopherol—a lipophilic form of vitamin E—is efficiently absorbed in the presence of dietary fats and transported via chylomicrons to tissues[67]. Similarly, raphanin, produced from glucosinolates through myrosinase action, is rapidly absorbed as an isothiocyanate but is also quickly metabolized[68], while beta-ionone, despite being absorbed via passive diffusion, faces constraints from first-pass metabolism and low aqueous solubility[69].

A higher Pa value indicates a greater likelihood that a compound will exhibit activity in the respective biological processes[70,71]. Kaempferol is involved in most of these activities, except for its antineoplastic effects in endocrine and thyroid cancers.

Endocrine resistance was identified as the most enriched pathway in our analysis, with the lowest FDR and highest –log10(p) value, strongly suggesting that RRM compounds interact with mechanisms driving endocrine treatment failure. This resistance is often associated with the activation of alternative signaling pathways (such as PI3K/AKT, MAPK, and mTOR) that bypass estrogen receptor signaling, along with alterations in growth factor receptors, co-regulators, and downstream transcription factors that promote continued cellular proliferation and survival. These findings indicate that RRM compounds may modulate these critical networks, warranting further investigation in relevant cancer models.

In addition, kaempferol demonstrates significant anticancer and antioxidant potential by modulating the cell cycle, apoptosis, proliferation, and angiogenesis, primarily via MAPK/ERK1/2, PI3K/Akt/mTOR, and VEGF pathways[72,73]. Similarly, kaempferitrin has shown considerable anticancer activity, with numerous studies

underscoring its effectiveness across various cancer types[74,75]. Preclinical studies have also shown that tocopherol modulates inflammation, oxidative stress, the cell cycle, and apoptosis through pathways such as NF-κB, MAPK, and PI3K/Akt/mTOR. Although clinical outcomes vary, tocopherol has been reported to improve redox and inflammatory status in metabolic conditions, while its effects on cancer remain inconsistent, demonstrating both pro- and anti-malignant outcomes[76].

Higher affinity corresponds to more stable drug-target interactions, thereby enhancing therapeutic potential[77]. Kaempferitrin's strong affinity for MAPK1 and SRC underscores its potential to modulate inflammation and cancer pathways, while its interactions with AKT1 and ESR1 further support its role as a multi-target agent with antioxidant, anti-inflammatory, and anticancer properties. Kaempferitrin may interact with AKT1 by modulating its phosphorylation status, thereby affecting oxidative stress resistance, inflammatory responses, and cancer cell survival. While further research is needed to fully elucidate its effects on AKT1 and its downstream targets, existing evidence suggests that kaempferitrin holds promise as a therapeutic agent for oxidative stress-related diseases, inflammation, and cancer.

Binding-free energy values further emphasize its ability to engage key proteins in these pathways. Specifically, kaempferitrin exhibited robust binding to AKT1 through van der Waals forces, hydrogen bonds, and pi interactions—stabilizing the complex via pi-alkyl, pi-pi stacking, and pi-anion interactions with critical residues. Van der Waals forces promote close packing and shape complementarity between the ligand and receptor, minimizing unfavorable interactions and enhancing specificity[78]. Additionally, pi interactions, particularly pi-alkyl and pi-pi stacking, contribute electronic stabilization and strengthen hydrophobic interactions within the complex[79].

The molecular docking results are strongly reinforced by the MD simulations, which confirm that AKT1 is robustly bound by kaempferitrin. Although some dynamic fluctuations are exhibited by the ligand, the protein–ligand interface is maintained in a consistently stable state by persistent hydrogen bonds, hydrophobic interactions, and water-mediated bridges. Furthermore, the overall structural integrity of the protein is supported by steady values in the radius of gyration, SASA, and energy profiles throughout the simulation. These findings validate the docking predictions and underscore the potential of kaempferitrin as a potent and selective AKT1 inhibitor, with promising implications for targeted drug design in the treatment of inflammation, oxidative stress, and cancer.

Drosophila melanogaster possesses an effective immune system that combats infections through two primary mechanisms: humoral and cellular responses[80]. The humoral response involves the production of antimicrobial peptides (AMPs) that disrupt microbial membranes to eliminate pathogens[81]. A critical aspect of this defense is the recognition of bacterial signals by peptidoglycan recognition proteins (PGRPs), which are essential for insect immunity[82]. In particular, PGRP-LB modulates immune responses by degrading peptidoglycan from Gram-negative bacteria, thereby balancing the immune deficiency (*Imd*) pathway and preventing excessive inflammation and tissue damage while maintaining effective bacterial resistance[81–83].

Dysregulation of *PGRP-LB* in Drosophila models such as Dm *PGRP-LBΔ* leads to elevated proinflammatory cytokines, indicative of chronic immune activation[82]. For example, overexpression of Diptericin A, encoded by the *dptA* gene, serves as a marker of *Imd* pathway overactivation, while elevated Turandot A levels, encoded by the *totA* gene and regulated by the JAK-STAT pathway, underscore the broader role of immune signaling in homeostasis. Moreover, Diptericin overexpression driven by NF-κB (Relish) overactivation has been linked to chronic inflammation, neurodegeneration, and reduced lifespan in flies[84], highlighting the delicate balance required within the immune system to protect against pathogens while minimizing long-term damage.

The lack of toxicity observed in the larvae may be attributed to beneficial compounds in the RRM extract, such as antioxidants and polyphenols, which support cellular health. These findings suggest that RRM extract is safe at the tested lower concentrations and does not adversely affect Dm *PGPR-LBΔ* development or viability[85]. One potential explanation for the reduced protective effects at higher doses is hormesis, where low concentrations produce beneficial outcomes while higher concentrations become toxic[86]. At elevated doses, the adverse effects of toxic constituents in the extract may surpass its protective benefits, leading to pathway saturation and off-target interactions that disrupt normal cellular functions[87]. Additionally, the synergistic effects observed at low doses may shift to antagonistic interactions at higher doses, further diminishing the overall efficacy[49]. These observations underscore the importance of careful dose optimization to fully leverage the protective potential of the plant extract.

The extract's protective properties likely derive from its bioactive compounds, which counteract the negative effects of HKE exposure and enhance larval resilience under stress. The observed dose-dependent response highlights the potential of RRM as a functional ingredient for boosting host defenses through immune modulation and stress mitigation. Supporting this, previous reports indicate that GABA in radish microgreens may contribute to improved immunity via broader immunomodulatory effects of the GABAergic system[88].

At the molecular level, HKE exposure triggered the expression of *dptA* and *totA* genes, whereas treatment with RRM extract significantly suppressed their expression. These results indicate that Dm *PGRP-LBΔ* modulates immune responses, potentially mitigating the adverse effects of excessive activation[89]. Notably, *totA* expression, which is regulated by the JAK-STAT pathway and typically elevated by oxidative stress such as that induced by HKE, was reduced by RRM extract—likely due to its antioxidant and anti-inflammatory properties—thereby enhancing cell survival and proliferation by reducing oxidative stress and apoptosis[90,91].

HKE treatment also increased reactive oxygen species (ROS) levels in larvae, further indicating oxidative stress[92]. SOD1 (Superoxide Dismutase 1) catalyzes the conversion of superoxide radicals into hydrogen peroxide, aiding in ROS neutralization[93]. In response to oxidative stress, cells upregulate SOD1 as an adaptive mechanism to protect against oxidative damage[94]. This upregulation of SOD1 is linked to reduced expression of the *totA* gene, which is associated with cell proliferation under ROS exposure[95,96]. The upregulation of sod1 gene expression in response to RRM extract suggests its role in mitigating oxidative stress, as SOD1 converts superoxide radicals

into H_2O_2, which is subsequently decomposed by enzymes such as catalase (CAT)[97]. Previous studies have demonstrated that overexpression of human SOD1 in *Drosophila* motor neurons can extend lifespan by up to 40%, restoring the shortened lifespan of Sod-null mutants—an effect attributed to improved reactive oxygen metabolism and increased resistance to oxidative stress[96].

Conversely, the downregulation of SOD2 and CAT, which are critical for mitochondrial ROS detoxification, suggests impaired conversion of H_2O_2 into water and oxygen, thereby reducing overall antioxidant capacity. SOD2 converts superoxide radicals to H_2O_2 in mitochondria[98], while CAT decomposes H_2O_2 into water and oxygen to protect against oxidative damage[99,100]. The observed decrease in *sod2* and *cat* expression in Dm *PGRP-LB$^\Delta$* larvae treated with RRM extract likely reflects mild oxidative stress and altered mitochondrial function. These findings underscore the complex relationship between antioxidant responses and phytochemical activity, with the reduction in *sod2* expression under elevated ROS conditions[101], indicating a regulatory mechanism worth further investigation.

At elevated doses, the extract may induce oxidative stress by overwhelming cellular antioxidant defenses and inhibiting the transcription or translation of related genes. This phenomenon may be linked to pro-oxidant phytochemicals, such as acylated pelargonidin derivatives found in red radish, which can act as either antioxidants or pro-oxidants depending on the prevailing conditions[102]. Moreover, the altered immune and oxidative stress responses in Dm PGRP-LBΔ larvae may increase sensitivity to the extract, potentially disrupting signaling pathways—such as NF-κB, JNK, or Nrf2—that regulate antioxidant gene expression. At lower concentrations, the antioxidant compounds in the extract may effectively scavenge ROS, reducing reliance on endogenous antioxidants like SOD2 and CAT, whereas higher concentrations may suppress these genes by interfering with regulatory pathways. These concentration-dependent effects appear to reflect a hormetic response, whereby low doses elicit protective antioxidant mechanisms and high doses trigger a pro-oxidant effect[103]. Specifically, a 1.25% concentration of the extract increases sod1 expression, enhancing cytoplasmic defense against superoxide radicals, while concurrently reducing *sod2* and *cat* expressions, which are involved in mitochondrial and peroxisomal detoxification of H_2O_2. These findings demonstrate a concentration-dependent regulation of antioxidant genes and suggest selective effects on oxidative stress pathways.

Despite the reduced expression of *sod2* and *cat* genes, 1.25% RRM extract does not induce overt toxicity in Dm *PGRP-LB$^\Delta$* larvae. The larvae appear to tolerate the induced oxidative stress, as evidenced by the absence of significant mortality or other signs of cellular damage. The lower expression of these genes may represent a mild oxidative stress response or an adaptive regulation of antioxidant defenses rather than an indication of toxicity. The relatively low ROS levels observed at this concentration suggest that the larvae's defense mechanisms are not overwhelmed, thereby preventing harmful effects. Overall, these results indicate that while the extract modulates oxidative stress pathways, it does not cause detrimental effects at the concentrations tested.

Both in silico and in vivo analyses provide robust evidence supporting the therapeutic potential of RRM extract. In silico studies reveal strong interactions between RRM extract and key human proteins (AKT1, ESR1, MAPK1, SRC, and TP53), which are critical regulators of cancer, inflammation, and oxidative stress. This suggests that RRM extract, particularly its bioactive component kaempferitrin, can influence apoptosis, immune signaling, and oxidative stress. In vivo experiments in Dm *PGRP-LB$^\Delta$* larvae corroborated these effects by demonstrating suppression of immune-related genes (*dptA* and *totA*) via NF-κB and JAK-STAT pathways, reduced ROS levels, and selective modulation of antioxidant-related genes (*sod1*, *sod2*, and *cat*). The alignment between in *silico* and in *vivo* findings reinforces the potential of RRM extract as a multifunctional agent with anti-inflammatory, antioxidant, and anticancer properties, thereby supporting its application in functional food development.

Methods
Preparation of red radish microgreens extract
The cultivation method for RRM followed our previous study[104]. The seeds (sourced from Known-You Seed, Thailand) were soaked in deionized water for 6 h, then sown on seedling trays and incubated in the dark for 3 days. After germination, the sprouts were grown into microgreens under LED lighting (7000 lx, 52–60% humidity, 26–26.5 °C) and harvested 7 days after seeding.

After harvesting, the RRM was microwave-dried until it reached a crisp texture. Extraction was performed using a modified microwave oven (Modena MV3002, 1440 W). Approximately 35.56 ± 0.22 g ($n = 6$) of dried microgreen was placed into a 500 ml round-bottom flask and wetted with about 50 ml of 96% ethanol. An additional 350–400 ml of 96% ethanol was added to the flask as the extraction solvent. The flask, containing the plant material and solvent, was attached to a condenser connected to the microwave oven. The extraction time was set for 5 min at 30% power (equivalent to 432 watts). The liquid extract was filtered using filter paper, yielding approximately 300 ml of extract. The extract was then concentrated using a rotary evaporator at a pressure of < 180 mbar and a temperature of 60 °C.

Metabolic profiling
The metabolic profiling of RRM extract was conducted using LC-HRMS and GC-MS. For the LC-HRMS analysis, liquid chromatography was performed with a Thermo Scientific™ Vanquish™ UHPLC Binary Pump, utilizing a ThermoScientific™ Accucore™ Phenyl-Hexyl column (100 mm × 2.1 mm ID × 2.6 μm). The mobile phase consisted of MS-grade water with 0.1% formic acid (Eluent A) and MS-grade methanol with 0.1% formic acid (Eluent B). The flow rate was 0.3 mL/min with a gradient from 95% Eluent A/5% Eluent B to 10% Eluent A/90% Eluent B over 25 min. The injection volume was 3 μL, and the column was maintained at 40 °C. Mass spectrometry was performed using the Thermo Scientific™ Q Exactive™ Hybrid Quadrupole-Orbitrap™ in ESI mode (positive/negative) with N2 as sheath, auxiliary, and sweep gases. The spray voltage was 3.30 kV, with a

capillary temperature of 320 °C and an auxiliary gas heater at 30 °C. The scan range was 66.7–1000 m/z, with resolutions of 70,000 for full MS and 17,600 for dd-MS2.

The analysis of RRM extracts using Gas Chromatography-Mass Spectrometry (GC-MS) was performed with a Perkin Elmer Clarus 500 gas chromatograph paired with a Perkin Elmer Clarus SQ 8 S mass spectrometer. A Perkin Elmer Elite-5ms capillary column (30 m length, 0.25 mm internal diameter, and 0.25 μm film thickness) was used. Electron ionization at 70 eV facilitated the mass spectrometer, with a scan range of 40 to 450 Da. Helium served as the carrier gas in split mode with a 10:1 ratio. The injector was set at 250 °C, with a 1 μL injection volume and a 2-minute solvent delay. The oven temperature program started at 110 °C (held for 2 min), followed by a ramp of 10 °C/min to 200 °C, and then 5 °C/min to 280 °C, with a 9-minute hold at the final temperature.

Metabolites data preprocessing

The LC-MS/MS data were processed following established protocols using Compound Discoverer 3.3 software (Thermo Fisher Scientific, USA)[104]. This workflow included peak extraction, alignment, and compound identification to ensure data accuracy and reliability. Raw data were imported and processed through multiple steps: peak extraction, retention time correction, adduct ion combination, missing value imputation, and background peak labeling. Metabolite identification was conducted using the BGI Library and mzCloud database, referencing molecular weight, retention time, peak area, and fragmentation patterns to enhance identification confidence.

Metabolites filtering

To identify unique compounds, duplicates from the LC-MS and GC-MS analyses were removed. The compounds were then filtered to differentiate between synthetic and naturally occurring substances. This process involved searching for compound names in several databases, such as PubChem[105], LOTUS: Natural Products Online, SuperNatural 3.0, and Dr. Duke's Phytochemical and Ethnobotanical Databases.

Network Pharmacology analysis

Identification of gene target

The process began with identifying the targets of the natural compounds. SMILES notations for the selected natural products were obtained from PubChem. These SMILES were then used in the SwissTargetPrediction server[106] to identify the associated protein targets. To ensure data accuracy and consistency, duplicate entries were eliminated when multiple compounds were linked to the same targets. Subsequently, genes associated with cancer, inflammation, and oxidative stress were identified using the GeneCards database[107], further refining the list of potential targets.

Protein–protein interaction and skyline query analyses

A Venn analysis was conducted in Microsoft Excel to identify genes shared between the target genes of RRM compounds and those linked to cancer, inflammation, and oxidative stress. The overlapping genes were visualized in a Venn diagram created in the same software. These shared genes were further analyzed to construct a protein-protein interaction (PPI) network using the STRING 11.5 database (https://www.string-db.org/) with a minimum interaction score threshold of 0.9, ensuring the highest level of confidence.

The network was analyzed using Cytoscape 3.10.2 [28] to evaluate its topology and compute centrality metrics for each gene. The MNC (Maximum Neighborhood Component) and MCC (Maximal Clique Centrality) algorithms, available through the cytoHubba plugin[108], were applied to identify the top 20 genes based on MNC and the top 20 genes based on MCC. The resulting networks were then integrated into a single network to remove redundancies.

Skyline query analysis was conducted to determine the five most dominant genes in comparison to the other top genes identified through MNC and MCC algorithms. The analysis utilized closeness, betweenness, degree, and stress centralities as parameters for skyline evaluation. Once identified, the compounds targeting these five key genes were cross-referenced with the existing dataset. Subsequently, the five principal compounds were identified based on their natural occurrence in Raphanus sativus and the number of genes they targeted among the five key genes.

Genes enrichment analysis

Gene enrichment analysis was performed to explore the biological processes associated with the five key genes. This analysis utilized the StringApp plugin for Cytoscape[109] and the Metascape web server[110]. Gene Ontology (GO) annotations for Biological Processes, Molecular Functions, and Cellular Components[111], along with KEGG pathway annotations[112] were emphasized. Visual representations of the GO and KEGG annotations were generated using the SRplot web server[113].

Prediction of pharmacokinetics, drug-likeness, and biological activities

Pharmacokinetics and drug-likeness assessments were conducted for the five principal compounds, focusing on ADMET (Absorption, Distribution, Metabolism, Excretion, and Toxicity) properties and Lipinski's Rule of Five[114]. These evaluations utilized the web servers admetSAR 1.0 (https://lmmd.ecust.edu.cn/admetsar1/)[115], ADMETlab 3.0 (https://admetlab3.scbdd.com/)[116], and ProTox III (https://tox.charite.de/protox3/)[117]. Additionally, the biological activity of the compounds was analyzed using the Way2Drug PASS online tool (https://www.way2drug.com/passonline/)[118]. Visualization of the biological activity data and their corresponding Pa (probability of activity) values was performed using the SRplot web server[113].

Molecular Docking

The molecular docking analysis was conducted to explore interactions between the protein structures of five key proteins (receptors) and five main chemical compounds (ligands), resulting in a total of 20 docking simulations. Additionally, native ligands of the receptors were redocked with their respective receptors to ensure the reliability of the docking procedure. The five proteins studied were AKT1, ESR1 (encoding the ER-alpha protein, PDB ID: 3ERT), MAPK1 (encoding the ERK2 protein, PDB ID: 1TVO), SRC (PDB ID: 2H8H), and TP53 (encoding the P53 protein, PDB ID: 8F2H). The corresponding protein structures and their PDB identifiers were obtained from the Protein Data Bank (PDB). For AKT1, homology modeling was performed in silico using the SWISS-MODEL platform[119], with the protein sequence retrieved from NCBI (Accession Number: NP_001369359.1). The modeling utilized the template of crystal structure of AKT1 in complex with covalent-allosteric AKT inhibitor 24b (PDB ID: 6HHJ), which featured three mutations and exhibited missing residues in certain non-terminal regions[120]. The structural validation of each receptor was performed using the MolProbity web server[121] by conducting a Ramachandran analysis.

The docking analysis of five key proteins was performed using five principal compounds: kaempferitrin (CID: 5486199), D-alpha-tocopherol (commonly known as alpha-tocopherol, CID: 14985), kaempferol (CID: 5280863), raphanin (CID: 6433206), and EN0350000 (also known as beta-Ionone, CID: 638014). These compounds were retrieved from PubChem in 3D .sdf format. The docking simulations were carried out using Gnina, a deep-learning molecular docking tool derived from Smina and AutoDock Vina[122]. Gnina is available on GitHub (https://github.com/gnina/gnina) and was executed on Google Colab with GPU runtime support.

Initial redocking using the co-crystallized ligands was carried out to confirm the reliability of the docking procedure, with the process deemed valid if the root-mean-square deviation (RMSD) of the best redocked complex was 2Å or less[61]. In each docking method, the grid box was configured using the "--autobox_ligand" parameter, which automatically adjusted the grid box to the binding site of the native ligand. Since the P53 protein lacks a native ligand, redocking was not performed. Instead, its active site was identified using the CASTp online server[123], and the grid box dimensions were determined using AutoDockTools v.1.5.7 [124]. The grid box dimensions were manually adjusted in the command using the "--center" and "--size" parameters rather than the "--autobox" option, ensuring precise ligand positioning.

Molecular docking data were selected and prioritized based on binding affinity, with the lowest binding-free energy (BFE) indicating the most favorable docked complexes. The interactions within these favorable complexes were visualized using Biovia Discovery Studio software.

Molecular dynamics (MD) simulations

Desmond from Schrödinger LLC was employed to run 100 ns MD simulations based on a previous procedure[125]. The selected proteins and ligands were optimized and energy-minimized using Maestro's Protein Preparation Wizard to remove steric clashes, poor contacts, and distorted geometries. The system was built using the System Builder tool with an orthorhombic TIP3P solvent model and the OPLS_2005 force field[126]. Counter ions were added to neutralize the models, and 0.15 M sodium chloride was introduced to simulate physiological conditions, maintained at 310 K and 1 atm. Trajectories were recorded every 100 ps, and protein–ligand stability was confirmed via root-meansquare deviation (RMSD) analysis over time. The measurements of the radius of gyration (Rg), solvent-accessible surface area (SASA), and hydrogen bonds for both the protein alone and its interactions with the ligand were performed using the GROMACS simulation package following standard procedures[127–129]. Additionally, binding-free energy was estimated using the MM-PBSA method by extracting frames at regular intervals to assess the stability of the ligand–protein interactions.

Preclinical validation using the Drosophila melanogaster PGPR-LB$^\Delta$

Drosophila melanogaster PGPR-LB$^\Delta$ (Dm *PGPR-LB$^\Delta$*) strain was obtained from the Host and Defense Laboratory at Kanazawa University in Japan. *Drosophila melanogaster* deficient in *PGRP-LB* demonstrate an elevated production of proinflammatory cytokines[82]. A 50% extract solution of RRM was prepared by dissolving 1.25 g of the extract in 2.5 mL of 70% ethanol, followed by dilution to achieve concentrations of 1.25%, 0.625%, and 0.312%. The insects were provided with a diet consisting of RRM, corn flour, granulated sugar, agar, and Miller Luria-Bertani broth (LBB) (HIMEDIA Lab Chemicals & Biochemicals, India).

Preparation of heat-killed Escherichia coli

E. coli FNCC 0091 was cultured in nutrient agar (NA) medium for 24 h. Following this incubation period, 2 mL of sterile water was added to the culture and incubated for an additional 2 h. The resulting sterile water containing *E. coli* was then transferred to LBB medium and incubated at 37 °C for 24 h while being agitated on a shaker. After incubation, the *E. coli* culture in LBB medium was subjected to autoclaving at 121 °C and 2 atm pressure for 30 min to deactivate the bacteria.

Preparation of Dm PGPR-LB$^\Delta$ feed containing heat-killed E. coli

The insect feed was formulated with a mixture of corn flour, sugar, and agar, and a heat-killed *E. coli* (HKE) solution. The feed was heated to 100 °C while being stirred until it reached a consistent and thickened texture. It was then placed into feeding tubes designated for the insects.

Toxicity test

A toxicity test was conducted to evaluate the viability of Dm *PGPR-LB$^\Delta$* following treatment with the various concentration of RMM's extract. Second-instar larvae of Dm *PGPR-LB$^\Delta$* were used across multiple treatment groups. The groups included: (1) a control group without any treatment, (2) a group treated with 70% ethanol, and (3) groups exposed to varying concentrations of RRM extract with three biological replications. Larval

Genes	Forward primers	Reverse primers
rp49	5′-GACGCTTCAAGGGACAGTATCTG-3′	5′-AAACGCGGTTCTGCATGAG-3′
dptA	5′-AGGTGTGGACCAGCGACAA-3′	5′-TGCTGTCCATATCCTCCATTCA-3′
totA	5′-GAATAGCCCATGCATAGAGGAC-3′	5′-CCAAAATGAATTCTTCAACTGCT-3′
sod1	5′-AGGTCAACATCACCGACTCC-3′	5′-GTTGACTTGCTCAGCTCGTG-3′
sod2	5′-TGGCCACATCAACCACAC-3′	5′-TTCCACTGCGACTCGATG-3′
cat	5′-TTCCTGGATGAGATGTCGCACT-3′	5′-TTCTGGGTGTGAATGAAGGTGG-3′

Table 5. Primers used in RT-qPCR analysis.

development was observed throughout the experimental period, specifically monitoring the progression from the larval to pupal stage and from pupal to adult fly.

Survival analysis
The survival test was designed to assess the growth of Dm *PGPR-LB^Δ* through its larval, pupal, and adult stages after administering HKE alone and in combination with various RRM extract. Second-instar larvae were monitored until they reached the adult stage, with each treatment condition replicated three times. Daily counts were recorded to track the number of larvae that progressed to pupae and subsequently to adult flies, with observations continuing until all adult insects had died.

Isolation of RNA for gene expression analysis
RNA isolation followed the spin column method (PureLink RNA Mini Kit, Invitrogen, Thermo Fisher Scientific Inc., Carlsbad), based on the manufacturer's protocol. Ten Dm *PGPR-LB^Δ* larvae per group were homogenized in 175 μl RNA lysis buffer. After adding 350 μl RNA dilution buffer, the mixture was inverted, incubated at 70 °C for 3 min, and centrifuged at 14,000 G for 10 min at 4 °C. The supernatant was transferred to a fresh microcentrifuge tube using a micropipette. Two hundred microliters of 95% ethanol were added and homogenized using a micropipette approximately 3–4 times. The mixture was then transferred to the spin column apparatus. Centrifugation was performed at 14,000 G for 1 min. The spin basket was removed from the spin column assembly, and the liquid in the collection tube was discarded. Subsequently, 600 μl of RNA wash solution was added to the spin column assembly and centrifuged at 14,000 G for 1 min.

The collection tube was emptied, and a DNase mixture was prepared by combining 40 μl of yellow core buffer, 5 μl of 0.09 M MnCl2, and 5 μl of DNase I enzyme, with the reaction volume increased by approximately 10%. This mixture was homogenized using a micropipette. Fifty microliters of the mixture were transferred to the spin basket. The assembly was incubated for 15 min at a temperature of 20–25 °C. Following incubation, 200 μl of DNase stop solution were added to the spin basket and centrifuged at 14,000 G for 1 min. The collection tube was not emptied for the subsequent step.

Next, 600 μl of RNA wash solution were added and centrifuged at 14,000 G for 1 min. The collection tube was emptied, and 250 μl of RNA wash solution were added, followed by centrifugation at 14,000 G for 2 min. The spin basket was then transferred from the collection tube to the elution tube (microtube), and 100 μl of nuclease-free water were added to the elution tube. The spin basket assembly was centrifuged at 14,000 G for 1 min. Finally, the spin basket was removed, and the elution tube containing the isolated RNA was stored at approximately − 80 °C.

Real-time reverse transcriptase PCR (RT-PCR)
Gene expression levels in Dm *PGPR-LB^Δ* were measured using RT-qPCR with the Universal One-Step RT-qPCR Kit (Luna, New England Biolabs, Inc., U.S.) based on the manufacturer's protocol, with slight modifications[130]. The RT-qPCR reactions were performed in a final volume of 10 μL. The cycling conditions included reverse transcription at 50°C for 10 minutes, followed by an initial enzyme activation step at 95°C for 2 minutes. Amplification was carried out for 40 cycles, with denaturation at 95°C for 10 seconds, annealing at 60°C for 30 seconds, and extension at 72°C for 30 seconds. A melt curve analysis was conducted to confirm the specificity of the amplified products, spanning a temperature range of 60°C to 95°C. The primer sequences used in this assay are provided in Table 5. Additionally, RNA levels of the target gene were assessed using rp49 primers as an internal reference for normalization. Gene expression analysis was performed using three biological replicates.

Nitroblue tetrazolium (NBT) assay
To quantify ROS in larval hemolymph, a nitroblue tetrazolium (NBT) reduction assay was performed as previously described[89,131]. In this assay, ROS reduce the yellow NBT dye into insoluble formazan particles that absorb at 595 nm. Fifty larvae were rinsed with phosphate-buffered saline (PBS) to eliminate food debris, and hemolymph was extracted on ice to prevent melanization. A 300 μL mixture was prepared by combining 100 μL hemolymph with 200 μL 1× PBS, then adding an equal volume of NBT solution. The mixture was incubated in the dark at room temperature for 1 h, after which 300 μL of 100% glacial acetic acid was added to stop the reaction. Following centrifugation at maximum speed for 1 min, absorbance at 595 nm was measured after the addition of 50% acetic acid.

Data analysis

All data were analyzed using GraphPad Prism 9. Each experiment, including survival assays and gene expression analyses, was performed with three replicates. Bar graphs were used to present the data, and one-way analysis of variance (ANOVA) was applied for statistical comparisons. Variability was assessed by calculating the standard deviation and 95% confidence intervals, and statistical significance was defined as a *p*-value of less than 0.05.

Data availability

References

1. Tallei, T. E. et al. A comprehensive review on the antioxidant activities and health benefits of microgreens: current insights and future perspectives. *Int. J. Food Sci. Technol.* **59**, 58–71 (2024).
2. Bowen-Forbes, C. et al. Broccoli, Kale, and radish sprouts: key phytochemical constituents and DPPH free radical scavenging activity. *Molecules* **28**, (2023).
3. Treasure, K., Harris, J. & Williamson, G. Exploring the anti-inflammatory activity of Sulforaphane. *Immunol. \& Cell. Biol.* **101**, 805–828 (2023).
4. Soundararajan, P. & Kim, J. S. Anti-Carcinogenic Glucosinolates in Cruciferous Vegetables and Their Antagonistic Effects on Prevention of Cancers. *Molecules* 23, (2018).
5. Fuente, B. et al. Antiproliferative effect of bioaccessible fractions of four Brassicaceae microgreens on human Colon cancer cells linked to their phytochemical composition. *Antioxidants (Basel Switzerland)* **9**, (2020).
6. Belošević, S. D. et al. Broccoli, Amaranth, and Red Beet Microgreen Juices: The Influence of Cold-Pressing on the Phytochemical Composition and the Antioxidant and Sensory Properties. *Foods* 13, null (2024).
7. Kurniati, D., Septiany, R. N., Lembong, E., Kayaputri, I. L. & Utama, G. L. Comparative study of phytochemical content, antioxidant, and anti-inflammatory properties of Merremia Hirta Merr. Mature plant and microgreen. *Nat Prod. Res* 1–9 https://doi.org/10.1080/14786419.2024.2425795
8. Bhattacharya, K. et al. Exploring the therapeutic potential of 8-Prenyldaidzein: A comprehensive study of its Multi-Target efficacy in Alzheimer's disease. *Curr. Alzheimer Res.* **21**, 578–598 (2024).
9. Khanal, P., Patil, V. S., Bhattacharya, K. & Patil, B. M. Multifaceted targets of Cannabidiol in epilepsy: modulating glutamate signaling and beyond. *Comput. Biol. Med.* **179**, 108898 (2024).
10. Khanal, P., Patil, V. S., Bhattacharya, K., Shrivastava, A. K. & Bhandare, V. V. Exploring the globoid cell leukodystrophy protein network and therapeutic interventions. *Sci. Rep.* **14**, 18067 (2024).
11. Bhattacharya, K. et al. Netting into the sophoretin pool: an approach to trace GSTP1 inhibitors for reversing chemoresistance. *Comput. Biol. Chem.* **108**, 107981 (2024).
12. Sailah, I. et al. A network Pharmacology approach to elucidate the anti-inflammatory and antioxidant effects of bitter leaf (Vernonia amygdalina Del). *Narra J.* **4**, e1016 (2024).
13. Noviandy, T. R. et al. An Explainable Multi-Model Stacked Classifier Approach for Predicting Hepatitis C Drug Candidates. *Sci* 6, (2024).
14. Maulana, A. et al. Machine learning approach for diabetes detection using Fine-Tuned XGBoost algorithm. *Infolitika J. Data Sci.* **1**, 1–7 (2023).
15. Bolus, H., Crocker, K., Boekhoff-Falk, G. & Chtarbanova, S. Modeling neurodegenerative disorders in Drosophila melanogaster. *Int J. Mol. Sci* **21**, (2020).
16. Vatashchuk, M. V., Bayliak, M. M., Hurza, V. V., Storey, K. B. & Lushchak, V. I. Metabolic Syndrome: Lessons from Rodent and Drosophila Models. *Biomed Res. Int.* 5850507 (2022). (2022).
17. Casas-Tintó, S. Drosophila as a Model for Human Disease: Insights into Rare and Ultra-Rare Diseases. *Insects* 15, (2024).
18. Henarejos-Castillo, I. et al. Whole-exome sequencing and Drosophila modelling reveal mutated genes and pathways contributing to human ovarian failure. *Reprod. Biol. Endocrinol.* **22**, 153 (2024).
19. Ogienko, A. A. et al. Drosophila as a model organism to study basic mechanisms of longevity. *Int J. Mol. Sci* **23**, (2022).
20. Obafemi, O. T. et al. Animal models in biomedical research: relevance of Drosophila melanogaster. *Heliyon* **11**, e41605 (2025).
21. Baenas, N. & Wagner, A. E. Drosophila melanogaster as an alternative model organism in nutrigenomics. *Genes Nutr.* **14**, 14 (2019).
22. Lopez-Ortiz, C. et al. Drosophila melanogaster as a translational model system to explore the impact of phytochemicals on human health. *Int J. Mol. Sci* **24**, (2023).
23. Alloggia, F. P., Bafumo, R. F., Ramirez, D. A., Maza, M. A. & Camargo, A. B. Brassicaceae microgreens: A novel and promissory source of sustainable bioactive compounds. *Curr. Res. Food Sci.* **6**, 100480 (2023).
24. Tallei, T. et al. A Comprehensive Review on the Antioxidant Activities and Health Benefits of Microgreens: Current Insights and Future Perspectives. *Int. J. Food Sci. & Technol.* null, null (2023).
25. Habtemariam, S. Anti-Inflammatory Therapeutic Mechanisms of Isothiocyanates: Insights from Sulforaphane. *Biomedicines* 12, (2024).
26. Olayanju, J. B., Bozic, D., Naidoo, U. & Sadik, O. A. *Comp. Rev. Key Isothiocyanates their Health Benefits Nutrients* **16**, (2024).
27. Shannon, P. et al. Cytoscape: A software environment for integrated models of biomolecular interaction networks. *Genome Res.* **13**, 2498 (2003).
28. Shannon, P. et al. Cytoscape: A software environment for integrated models. *Genome Res.* **13**, 426 (2003).
29. Fatimawali et al. Molecular insight into the Pharmacological potential of Clerodendrum Minahassae leaf extract for Type-2 diabetes management using the network Pharmacology approach. *Medicina (B Aires)* **59**, (2023).
30. Pendong, C. H. A., Suoth, E. J., Fatimawali, F & Tallei, T. E. Network Pharmacology approach to Understanding the antidiabetic effects of pineapple Peel hexane extract. *Malacca Pharm.* **2**, 24–32 (2024).
31. Wawo, A. E., Simbala, H. E. I., Fatimawali, F. & Tallei, T. E. A comprehensive network Pharmacology study on the Diabetes-Fighting capabilities of Yacon leaf extract. *Malacca Pharm.* **2**, 41–51 (2024).
32. Corcoran, C. A., Huang, Y. & Sheikh, M. S. The regulation of energy generating metabolic pathways by p53. *Cancer Biol. Ther.* **5**, 1610–1613 (2006).
33. Luo, J. et al. SRC kinase-mediated signaling pathways and targeted therapies in breast cancer. *Breast Cancer Res.* **24**, 99 (2022).
34. Huang, P., Han, J. & Hui, L. MAPK signaling in inflammation-associated cancer development. *Protein Cell.* **1**, 218–226 (2010).
35. Bhave, M. A. et al. Comprehensive genomic profiling of ESR1, PIK3CA, AKT1, and PTEN in HR(+)HER2(−) metastatic breast cancer: prevalence along treatment course and predictive value for endocrine therapy resistance in real-world practice. *Breast Cancer Res. Treat.* **207**, 599–609 (2024).

36. Glaviano, A. et al. PI3K/AKT/mTOR signaling transduction pathway and targeted therapies in cancer. *Mol. Cancer*. **22**, 138 (2023).
37. Chen, B., Ning, K., Sun, M. L. & Zhang, X. A. Regulation and therapy, the role of JAK2/STAT3 signaling pathway in OA: a systematic review. *Cell. Commun. Signal.* **21**, 67 (2023).
38. Li, Y., Wang, C., Gao, Y. & Zhou, L. Identification and Validation of PIK3CA as a Marker Associated with Prognosis and Immune Infiltration in Renal Clear Cell Carcinoma. *J. Oncol.* 3632576 (2021). (2021).
39. Manzoor, Z. & Koh, Y. S. Mitogen-activated protein kinases in inflammation. *J. Bacteriol. Virol.* **42**, 189–195 (2012).
40. Cargnello, M. & Roux, P. P. Activation and function of the MAPKs and their substrates, the MAPK-Activated protein kinases. *Microbiol. Mol. Biol. Rev.* **75**, 50–83 (2011).
41. Schroeder, H. T., De Lemos Muller, C. H., Heck, T. G. & Krause, M. Homem de Bittencourt, P. I. The dance of proteostasis and metabolism: unveiling the caloristatic controlling switch. *Cell. Stress Chaperones.* **29**, 175–200 (2024).
42. Rascio, F. et al. The pathogenic role of PI3K/AKT pathway in Cancer onset and drug resistance: an updated review. *Cancers (Basel)* 13, (2021).
43. Mangiapane, L. R. et al. PI3K-driven HER2 expression is a potential therapeutic target in colorectal cancer stem cells. *Gut* **71**, 119–128 (2022).
44. Prahallad, A. et al. PTPN11 is a central node in intrinsic and acquired resistance to targeted Cancer drugs. *Cell. Rep.* **12**, 1978–1985 (2015).
45. Tomuleasa, C. et al. Therapeutic advances of targeting receptor tyrosine kinases in cancer. *Signal. Transduct. Target. Ther.* **9**, 201 (2024).
46. Kontzias, A., Laurence, A., Gadina, M. & O'Shea, J. J. Kinase inhibitors in the treatment of immune-mediated disease. *F1000 Med. Rep.* **4**, 5 (2012).
47. Deng, S. et al. PI3K/AKT signaling tips the balance of cytoskeletal forces for Cancer progression. *Cancers (Basel)* **14**, (2022).
48. Ullah, A. et al. Bioactive Compounds in Citrus reticulata Peel Are Potential Candidates for Alleviating Physical Fatigue through a Triad Approach of Network Pharmacology, Molecular Docking, and Molecular Dynamics Modeling. *Nutrients* 16, (2024).
49. Chaachouay, N. & Synergy Additive effects, and antagonism of drugs with plant bioactive compounds. *Drugs Drug Candidates* **4**, (2025).
50. Li, Q. et al. Signaling pathways involved in colorectal cancer: pathogenesis and targeted therapy. *Signal. Transduct. Target. Ther.* **9**, 266 (2024).
51. Canesin, G., Krzyzanowska, A., Hellsten, R. & Bjartell, A. Cytokines and Janus kinase/signal transducer and activator of transcription signaling in prostate cancer: overview and therapeutic opportunities. *Curr. Opin. Endocr. Metab. Res.* **10**, 36–42 (2020).
52. Liu, H. M. et al. Possible mechanisms of oxidative Stress-Induced skin cellular senescence, inflammation, and Cancer and the therapeutic potential of plant polyphenols. *Int J. Mol. Sci* **24**, (2023).
53. Keewan, E. & Matlawska-Wasowska, K. The emerging role of suppressors of cytokine signaling (SOCS) in the development and progression of leukemia. *Cancers (Basel)* 13, (2021).
54. Unterlander, N., Mats, L., McGary, L. C., Gordon, H. O. W. & Bozzo, G. G. Correction to: Kaempferol rhamnoside catabolism in rosette leaves of senescing Arabidopsis and postharvest stored radish. *Planta* **256**, 48 (2022).
55. Hussain, M. S. et al. Kaempferol: paving the path for advanced treatments in aging-related diseases. *Exp. Gerontol.* **188**, 112389 (2024).
56. Zhong, Y. et al. Comparative analysis of volatile compounds from four radish microgreen cultivars based on ultrasonic cell disruption and HS-SPME/GC-MS. *Int J. Mol. Sci* **24**, (2023).
57. IVÁNOVICS, G. & HORVÁTH, S. Raphanin, an antibacterial principle of the radish (Raphanus sativus). *Nature* **160**, 297–298 (1947).
58. Gamba, M. et al. Nutritional and phytochemical characterization of radish (Raphanus sativus): A systematic review. *Trends Food Sci. Technol.* **113**, 205–218 (2021).
59. Sharma, S. et al. Vegetable microgreens: the Gleam of next generation super foods, their genetic enhancement, health benefits and processing approaches. *Food Res. Int.* **155**, 111038 (2022).
60. Vlachou, A., Doulkeridis, C., Rocha-Junior, J. B. & Nørvåg, K. Decisive skyline queries for truly balancing multiple criteria. *Data Knowl. Eng.* **147**, 102206 (2023).
61. Tallei, T. E. et al. Potential of plant bioactive compounds as SARS-CoV-2 main protease (Mpro) and spike (S) glycoprotein inhibitors: A molecular docking study. *Scientifica (Cairo).* 6307457 (2020). (2020).
62. Dutta, M. et al. Appraisals of the Bangladeshi medicinal plant Calotropis gigantea used by folk medicine practitioners in the management of COVID-19: A biochemical and computational approach. *Front Mol. Biosci* 8, (2021).
63. Beutler, J. A. Natural products as a foundation for drug discovery. *Curr. Protoc. Pharmacol.* **86**, e67 (2019).
64. Ali, A. et al. In Silico analysis and molecular Docking studies of natural compounds of Withania somnifera against bovine NLRP9. *J. Mol. Model.* **29**, 171 (2023).
65. Mousavi, S. S. et al. In Silico evaluation of Iranian medicinal plant phytoconstituents as inhibitors against main protease and the receptor-binding domain of SARS-CoV-2. *Molecules* **26**, 5724 (2021).
66. Singh, T. et al. The role of phytonutrient Kaempferol in the prevention of Gastrointestinal cancers: recent trends and future perspectives. *Cancers (Basel)* **16**, (2024).
67. Schubert, M. et al. Long-Chain metabolites of vitamin E: metabolic activation as a general concept for Lipid-Soluble vitamins? *Antioxidants (Basel Switzerland)* **7**, (2018).
68. Hoch, C. C. et al. Isothiocyanates in medicine: A comprehensive review on phenylethyl-, allyl-, and benzyl-isothiocyanates. *Pharmacol. Res.* **201**, 107107 (2024).
69. Zhu, X. & Zhu, G. The interaction between beta-ionone and 2-hydroxypropyl-beta-cyclodextrin during the formation of the inclusion complex. *Comput. Theor. Chem.* **1241**, 114937 (2024).
70. Wicaksono, D. et al. Elucidation of anti-human melanoma and anti-aging mechanisms of compounds from green seaweed Caulerpa racemosa. *Sci. Rep.* **14**, 27534 (2024).
71. Leonardo, J. et al. Unraveling biomolecules, antidiabetic and antioxidants properties of delitestm via pharmacoinformatics and in vitro investigation. *Pharmacol. Res. - Mod. Chin. Med.* **13**, 100551 (2024).
72. Qattan, M. Y. et al. Therapeutic importance of Kaempferol in the treatment of Cancer through the modulation of cell signalling pathways. *Molecules* **27**, (2022).
73. Shahbaz, M. et al. Anticancer, antioxidant, ameliorative and therapeutic properties of Kaempferol. *Int. J. Food Prop.* **26**, 1140–1166 (2023).
74. Su, M. et al. Kaempferitrin, a major compound from ethanol extract of Chenopodium ambrosioides, exerts antitumour and hepatoprotective effects in the mice model of human liver cancer xenografts. *J. Pharm. Pharmacol.* **75**, 1066–1075 (2023).
75. Zhou, S. et al. Potential anti-liver cancer targets and mechanisms of Kaempferitrin based on network pharmacology, molecular Docking and experimental verification. *Comput. Biol. Med.* **178**, 108693 (2024).
76. Ungurianu, A., Zanfirescu, A., Nițulescu, G. & Margină, D. Vitamin E beyond Its Antioxidant Label. *Antioxidants* 10, (2021).
77. Du, X. et al. Insights into Protein-ligand interactions: mechanisms, models, and methods. *Int J. Mol. Sci* **17**, (2016).

78. Bitencourt-Ferreira, G., Veit-Acosta, M. & de Azevedo, W. F. Springer New York, Van der Waals Potential in Protein Complexes BT - Docking Screens for Drug Discovery. in (ed. de Azevedo Jr., W. F.) 79–91 (2019). https://doi.org/10.1007/978-1-4939-9752-7_6

79. Chen, T., Li, M. & Liu, J. π–π stacking interaction: A nondestructive and facile means in material engineering for bioapplications. *Cryst. Growth Des.* **18**, 2765–2783 (2018).

80. Duarte-Mata, D. I. & Salinas-Carmona, M. C. Antimicrobial peptides´ immune modulation role in intracellular bacterial infection. *Front. Immunol.* **14**, 1119574 (2023).

81. Royet, J., Gupta, D. & Dziarski, R. Peptidoglycan recognition proteins: modulators of the Microbiome and inflammation. *Nat. Rev. Immunol.* **11**, 837–851 (2011).

82. Orlans, J. et al. PGRP-LB: an inside view into the mechanism of the amidase reaction. *Int J. Mol. Sci* **22**, (2021).

83. Buchon, N., Silverman, N. & Cherry, S. Immunity in Drosophila melanogaster–from microbial recognition to whole-organism physiology. *Nat. Rev. Immunol.* **14**, 796–810 (2014).

84. Hanson, M. A., Grollmus, L. & Lemaitre, B. Ecology-relevant bacteria drive the evolution of host antimicrobial peptides in Drosophila. *BioRxiv* https://doi.org/10.1101/2022.12.23.521774 (2023).

85. Dubey, I., Khan, S. & Kushwaha, S. Developmental and reproductive toxic effects of exposure to microplastics: A review of associated signaling pathways. *Front. Toxicol.* **4**, 901798 (2022).

86. Bondy, S. C. The Hormesis Concept: Strengths and Shortcomings. *Biomolecules* 13, (2023).

87. Nunes, D. R., da Monteiro, C. M. A. & Dos Santos, J. L. C. S. de J. Herb-Induced Liver Injury-A Challenging Diagnosis. *Healthc. (Basel, Switzerland)* 10, (2022).

88. Shan, Y. et al. Understanding the function of the GABAergic system and its potential role in rheumatoid arthritis. *Front Immunol* **14**, (2023).

89. Hardiyanti, W. et al. Evaluating the impact of vitamin D(3) on NF-κB and JAK/STAT signaling pathways in Drosophila melanogaster. *ACS Omega.* **9**, 20135–20141 (2024).

90. Sun, G., Ding, X. A., Argaw, Y., Guo, X. & Montell, D. J. Akt1 and dCIZ1 promote cell survival from apoptotic caspase activation during regeneration and oncogenic overgrowth. *Nat. Commun.* **11**, 5726 (2020).

91. Kinoshita, Y., Shiratsuchi, N., Araki, M. & Inoue, Y. H. Anti-Tumor Effect of Turandot Proteins Induced via the JAK/STAT Pathway in the mxc Hematopoietic Tumor Mutant in Drosophila. *Cells* 12, (2023).

92. Jomova, K. et al. Reactive oxygen species, toxicity, oxidative stress, and antioxidants: chronic diseases and aging. *Arch. Toxicol.* **97**, 2499–2574 (2023).

93. Wang, Y., Branicky, R., Noë, A. & Hekimi, S. Superoxide dismutases: dual roles in controlling ROS damage and regulating ROS signaling. *J. Cell. Biol.* **217**, 1915–1928 (2018).

94. Watanabe, K. et al. Superoxide dismutase 1 loss disturbs intracellular redox signaling, resulting in global age-related pathological changes. *Biomed Res. Int.* 140165 (2014). (2014).

95. Tsang, C. K., Liu, Y., Thomas, J., Zhang, Y. & Zheng, X. F. Superoxide dismutase 1 acts as a nuclear transcription factor to regulate oxidative stress resistance. *Nat. Commun.* **5**, 3446 (2014).

96. Parkes, T. L. et al. Extension of Drosophila lifespan by overexpression of human SOD1 in motorneurons. *Nat. Genet.* **19**, 171–174 (1998).

97. Olufunmilayo, E. O., Gerke-Duncan, M. B. & Holsinger, R. M. D. Oxidative stress and antioxidants in neurodegenerative disorders. *Antioxidants (Basel Switzerland)* **12**, (2023).

98. Andrés, C. M. C., de la Lastra, J. M., Juan, C. A., Plou, F. J. & Pérez-Lebeña, E. Chemistry of hydrogen peroxide formation and elimination in mammalian cells, and its role in various pathologies. *Stresses* **2**, 256–274 (2022).

99. Hadwan, M. H. et al. An improved method for measuring catalase activity in biological samples. *Biol. Methods Protoc.* **9**, bpae015 (2024).

100. Jomova, K. et al. Several lines of antioxidant defense against oxidative stress: antioxidant enzymes, nanomaterials with multiple enzyme-mimicking activities, and low-molecular-weight antioxidants. *Arch. Toxicol.* **98**, 1323–1367 (2024).

101. Zheng, M. et al. The applications and mechanisms of superoxide dismutase in medicine, food, and cosmetics. *Antioxidants (Basel Switzerland)* **12**, (2023).

102. Wang, L. S. et al. Antioxidant and pro-oxidant properties of acylated pelargonidin derivatives extracted from red radish (Raphanus sativus Var. Niger, Brassicaceae). *Food Chem. Toxicol.* **48**, 2712–2718 (2010).

103. Wan, Y. et al. Current advances and future trends of hormesis in disease. *Npj Aging.* **10**, 26 (2024).

104. Tallei, T. E. et al. A comparative analysis on impact of drying methods on metabolite composition in broccoli microgreens. *LWT* **210**, 116866 (2024).

105. Kim, S. et al. PubChem 2023 update. *Nucleic Acids Res.* **51**, D1373–D1380 (2023).

106. Daina, A., Michielin, O. & Zoete, V. SwissTargetPrediction: updated data and new features for efficient prediction of protein targets of small molecules. *Nucleic Acids Res.* **47**, W357–W364 (2019).

107. Stelzer, G. et al. The GeneCards suite: From gene data mining to disease genome sequence analyses. *Curr. Protoc. Bioinforma.* 1.30.1–1.30.33 (2016). (2016).

108. Chin, C. H. et al. CytoHubba: identifying hub objects and sub-networks from complex interactome. *BMC Syst. Biol.* **8** (Suppl 4), S11 (2014).

109. Doncheva, N. T., Morris, J. H., Gorodkin, J. & Jensen, L. J. Cytoscape StringApp: network analysis and visualization of proteomics data. *J. Proteome Res.* **18**, 623–632 (2019).

110. Zhou, Y. et al. Metascape provides a biologist-oriented resource for the analysis of systems-level datasets. *Nat. Commun.* **10**, 1523 (2019).

111. Ge, S. X., Jung, D. & Yao, R. ShinyGO: a graphical gene-set enrichment tool for animals and plants. *Bioinformatics* **36**, 2628–2629 (2020).

112. Kanehisa, M., Sato, Y., Kawashima, M., Furumichi, M. & Tanabe, M. KEGG as a reference resource for gene and protein annotation. *Nucleic Acids Res.* **44**, D457–D462 (2016).

113. Tang, D. et al. SRplot: A free online platform for data visualization and graphing. *PLoS One.* **18**, 1–8 (2023).

114. Lipinski, C. A. Rule of five in 2015 and beyond: target and ligand structural limitations, ligand chemistry structure and drug discovery project decisions. *Adv. Drug Deliv. Rev.* **101**, 34–41 (2016).

115. Cheng, F. et al. AdmetSAR: a comprehensive source and free tool for assessment of chemical ADMET properties. *J. Chem. Inf. Model.* **52**, 3099–3105 (2012).

116. Fu, L. et al. ADMETlab 3.0: an updated comprehensive online ADMET prediction platform enhanced with broader coverage, improved performance, API functionality and decision support. *Nucleic Acids Res.* **52**, W422–W431 (2024).

117. Banerjee, P., Kemmler, E., Dunkel, M. & Preissner, R. ProTox 3.0: a webserver for the prediction of toxicity of chemicals. *Nucleic Acids Res.* **52**, W513–W520 (2024).

118. Filimonov, D. A. et al. Prediction of the biological activity spectra of organic compounds using the pass online web resource. *Chem. Heterocycl. Compd.* **50**, 444–457 (2014).

119. Waterhouse, A. et al. SWISS-MODEL: homology modelling of protein structures and complexes. *Nucleic Acids Res.* **46**, W296–W303 (2018).

120. Uhlenbrock, N. et al. Structural and chemical insights into the covalent-allosteric Inhibition of the protein kinase Akt. *Chem. Sci.* **10**, 3573–3585 (2019).

121. Chen, V. B. et al. MolProbity: all-atom structure validation for macromolecular crystallography. *Acta Crystallogr. D Biol. Crystallogr.* **66**, 12–21 (2010).
122. McNutt, A. T. et al. GNINA 1.0: molecular Docking with deep learning. *J. Cheminform.* **13**, 43 (2021).
123. Tian, W., Chen, C., Lei, X., Zhao, J. & Liang, J. CASTp 3.0: computed atlas of surface topography of proteins. *Nucleic Acids Res.* **46**, W363–W367 (2018).
124. Morris, G. M. et al. Software news and updates AutoDock4 and AutoDockTools4: automated Docking with selective receptor flexibility. *J. Comput. Chem.* **30**, 2785–2791 (2009).
125. Kandeel, M. et al. Comprehensive in Silico analyses of flavonoids elucidating the drug properties against kidney disease by targeting AIM2. *PLoS One.* **18**, e0285965 (2023).
126. Shivakumar, D. et al. Prediction of absolute solvation free energies using molecular dynamics free energy perturbation and the OPLS force field. *J. Chem. Theory Comput.* **6**, 1509–1519 (2010).
127. Celik, I. & Tallei, T. E. A computational comparative analysis of the binding mechanism of Molnupiravir's active metabolite to RNA-dependent RNA polymerase of wild-type and Delta subvariant AY.4 of SARS-CoV-2. *J. Cell. Biochem.* **123**, 807–818 (2022).
128. Celik, I., Abdellattif, M. H. & Tallei, T. E. An insight based on computational analysis of the interaction between the receptor-binding domain of the Omicron variants and human angiotensin-converting enzyme 2. *Biology (Basel)* **11**, (2022).
129. Hessel, S. S. et al. A computational simulation appraisal of banana lectin as a potential anti-SARS-CoV-2 candidate by targeting the receptor-binding domain. *J. Genet. Eng. Biotechnol.* **21**, 148 (2023).
130. Azmin, M. R., Habibie, H., Filmaharani, F., Roosevelt, A., Nurhidayah, A., Pratama, M. R., Hardiyanti, W., Latada, N. P., Mudjahid, M., Yuliana, D., & Nainu, F. (2025). Aspirin-Mediated Reduction of Glucose Level and Inflammation in Drosophila melanogaster. ACS omega, 10(18), 18622–18628. https://doi.org/10.1021/acsomega.4c11509
131. Nayak, N. & Mishra, M. Estimation of Oxidative Stress and Survivorship in Drosophila BT - Fundamental Approaches to Screen Abnormalities in Drosophila. in (ed. Mishra, M.) 123–134 (Springer US, 2020). https://doi.org/10.1007/978-1-4939-9756-5_11.

Declarations

Competing interests

The authors declare no competing interests.

Additional information

Supplementary Information The online version contains supplementary material available at https://doi.org/10.1038/s41598-025-02999-5.

Correspondence and requests for materials should be addressed to T.E.T. or B.K.

Reprints and permissions information is available at www.nature.com/reprints.

Publisher's note Springer Nature remains neutral with regard to jurisdictional claims in published maps and institutional affiliations.